



## RESEARCH ARTICLE

10.1029/2020JD034432

# Observation of Terrestrial Gamma-Ray Flashes at Mid Latitude

### Key Points:

- First observation of Terrestrial Gamma-ray Flashes (TGFs) at latitudes greater than  $\pm 38^\circ$
- The associated storms show convection with overshooting tops, but not extreme meteorological conditions
- Changes in tropopause height with latitude is a major contribution but does not fully account for the rarity of mid latitude TGFs

C. Maiorana<sup>1</sup> , M. Marisaldi<sup>1,2</sup> , M. Füllekrug<sup>3</sup> , S. Soula<sup>4</sup> , J. Lapierre<sup>5</sup> ,  
A. Mezentsev<sup>1</sup> , C. A. Skeie<sup>1</sup> , M. Heumesser<sup>6</sup> , O. Chanrion<sup>6</sup> , N. Østgaard<sup>1</sup> ,  
T. Neubert<sup>6</sup>, and V. Reglero<sup>7</sup>

<sup>1</sup>Birkeland Centre for Space Science, Department of Physics and Technology, University of Bergen, Bergen, Norway, <sup>2</sup>INAF-OAS Bologna, Bologna, Italy, <sup>3</sup>Department of Electronic and Electrical Engineering, Centre for Space, Atmospheric and Oceanic Science, University of Bath, Bath, UK, <sup>4</sup>Laboratory of Aerology, University of Toulouse/CNRS, Toulouse, France, <sup>5</sup>Earth Networks, Germantown, MD, USA, <sup>6</sup>National Space Institute, Technical University of Denmark (DTU Space), Kongens Lyngby, Denmark, <sup>7</sup>Image Processing Laboratory, University of Valencia, Valencia, Spain

### Supporting Information:

Supporting Information may be found in the online version of this article.

### Correspondence to:

C. Maiorana,  
[Carolina.Maiorana@uib.no](mailto:Carolina.Maiorana@uib.no)

### Citation:

Maiorana, C., Marisaldi, M., Füllekrug, M., Soula, S., Lapierre, J., Mezentsev, A., et al. (2021). Observation of Terrestrial Gamma-ray Flashes at mid latitude. *Journal of Geophysical Research: Atmospheres*, 126, e2020JD034432. <https://doi.org/10.1029/2020JD034432>

Received 17 DEC 2020

Accepted 18 AUG 2021

**Abstract** We present a sample of Terrestrial Gamma-ray Flashes (TGFs) observed at mid latitudes by the Atmosphere Space Interaction Monitor (ASIM). The events were detected between June 2018 and August 2020 in the latitude bands between  $35^\circ$  and  $51^\circ$  in both hemispheres, which we hereafter refer to as “mid latitudes.” The sample includes the first observations above  $\pm 38^\circ$  and consists of 14 events clustered in four geographical regions: north-west Atlantic and eastern USA; Mediterranean Sea; the ocean around South Africa; and north-eastern China and Siberia. We examine the characteristics of each event, both standalone and in the context of the global ASIM TGF data set, and we find that our sample is consistent with the global population concerning the number of counts, but shows significantly shorter durations. We analyze the meteorological context and the general evolution of the parent storms and we show that the storms are not extreme in terms of total duration and extension. Whenever possible, we also include the radio sferics and the peak current of the parent stroke. Finally, we present an estimation of the TGF occurrence rate at mid latitudes, based on ASIM’s exposure, the local flash rate and tropopause altitude, and we show that it is outside but very close to two standard deviation from the rate of production at tropical latitudes, corrected by the higher atmospheric absorption of higher latitudes. This means that atmospheric absorption plays a major role in the detection of TGFs at mid latitudes, but we cannot rule out other factors.

## 1. Introduction

Terrestrial Gamma-ray Flashes (TGFs) are short bursts of gamma radiation originating from thunderclouds. They were discovered by the Burst and Transient Source Experiment (BATSE) instrument onboard Compton Gamma-Ray Observatory (Fishman et al., 1994) and have been detected and studied by the Reuven Ramaty High Energy Solar Spectroscopic Imager (RHESSI) (Smith et al., 2005), Astro-rivelatore Gamma a Immagini Leggero (AGILE) (Marisaldi et al., 2010), Fermi (Briggs et al., 2013) and Atmosphere Space Interaction Monitor (ASIM) (Neubert et al., 2019). ASIM is the first mission specifically designed for the study of TGFs and Transient Luminous Events (TLEs). It is placed on the International Space Station (ISS) and as such can for the first time detect TGF events up to  $\pm 51$  degrees in latitude.

Of the past missions, RHESSI had the highest orbital inclination:  $38^\circ$ . Smith et al. (2010) and Gjesteland et al. (2015) reported a few observations of TGFs occurring at around  $37^\circ$ , over the northern Atlantic ocean and over the Mediterranean Sea, which are the highest latitudes investigated to date and also the only observations of mid latitude TGFs until now. In the following, we consider the latitude bands between  $+35^\circ$  and  $+51^\circ$  and between  $-35^\circ$  and  $-51^\circ$  of latitude. The limit of  $51^\circ$  refers to ASIM’s footprint only: Due to their field of view, the MMIA instrument (see Section 2) can detect events up to around  $52^\circ$  and the MXGS instruments reaches up to  $60^\circ$  of latitude. Thus, our domain of study includes a large part of the mid latitudes for meteorology reference, which are between about  $30^\circ$  and  $60^\circ$  on both hemispheres. We will then refer to our domain as “mid latitude” for better readability, even if it is a subset of the traditional definition.

© 2021. The Authors.

This is an open access article under the terms of the [Creative Commons Attribution-NonCommercial-NoDerivs License](https://creativecommons.org/licenses/by/4.0/), which permits use and distribution in any medium, provided the original work is properly cited, the use is non-commercial and no modifications or adaptations are made.

TGFs are known to be produced by storms exhibiting a wide range of features (Chronis et al., 2016; Ursi et al., 2019), but most previous studies were based on equatorial and tropical data, as mid latitudes were only and partially accessible to RHESSI. Events produced in mid latitude bands are associated with mid latitude thunderstorms, which have a shorter vertical extension than the storms produced by deep convection at equatorial and tropical latitudes. This is due to the lower altitude of the tropopause at those latitudes and means the TGFs have to cross a thicker air column, thus experiencing more photon absorption on their path to the detector (Smith et al., 2010; Williams et al., 2006). For this reason, TGFs at mid latitudes are thought to be more difficult to detect. Smith et al. (2010) investigates this very hypothesis by comparing the geographic distribution of their sample with LIS/OTD maps and find only partial support, allowing for further studies.

The aim of this study is then to assess the rarity of TGFs at mid latitude, in comparison with the low-latitudes and with the global lightning distribution, and to see whether a pattern emerges in the characteristics of the storms that produced our sample and in the associated lightning.

We describe the ASIM instrument and all data sets used in Section 2. Section 3 details the methods used to associate a lightning stroke to the TGFs and to calculate the TGF-to-lightning ratio (TLR) at equatorial and mid latitudes. General results and three cases studies are presented in Section 4 and discussed in Section 5. Section 6 summarizes the conclusions of this work.

## 2. Instruments and Data

### 2.1. ASIM

Launched on April 2018 and installed on the ISS, ASIM is the first instrument specifically designed for the study of TGFs, TLEs and other thunderstorm-related phenomena (Neubert et al., 2019). The scientific payload consists of two main instruments: the Modular X- and Gamma-ray Sensor MXGS (Østgaard, Balling et al., 2019; Østgaard, Neubert et al., 2019) and the Modular Multi-spectral Imaging Array MMIA (Chanrion et al., 2019). The MXGS is further divided into two instruments: the High Energy Detector (HED), sensitive to photons with energies from 300 keV to more than 30 MeV, and the Low Energy Detector (LED), which covers the range from 50 to 400 keV. They are both used in the detection of TGFs, but the LED is also used for the imaging and the reconstruction of the direction of arrival of the photons by means of a coded mask system; moreover, it is only active on the nightside. LED consists of Cadmium-Zinc-Telluride crystals with 16,384 pixels. HED is always active, except during the passage through the South Atlantic Anomaly (SAA). It consists of 12 Bismuth-Germanium Oxide (BGO) scintillators organized in groups of 3 bars, each connected to a photomultiplier tube. The MMIA is an optical detector used for detecting TLEs and lightning flashes. It includes two cameras, one imaging at 337.0 nm, the other at 777.4 nm, and three photometers sensitive in three different wavelength bands: 777.4, 337 and 180–240 nm. MMIA only observes at night, therefore providing data only for three of the 14 TGFs. The MXGS and MMIA is a cross-triggering system, aiming at recording both the TGF and any simultaneous optical data; the relative timing accuracy between MXGS and MMIA is  $\pm 80 \mu\text{s}$  for events before April 2019 and  $\pm 5 \mu\text{s}$  after.

In the period between June 2018 and August 2020, ASIM detected 14 TGFs at mid latitude out of a global sample of more than 700 TGFs. Figure 1 shows a map of the world with the locations of the events marked in red. Their main characteristics are presented in Table 1.

### 2.2. Lightning and Radio Data

Lightning data were obtained from several detection networks: the Earth Networks Total Lightning Network (ENTLN), the World Wide Lightning Location Network (WWLLN) (Rodger et al., 2009) and the Global Lightning Data set (GLD360). These global networks use tens to hundreds radio sensors deployed worldwide to track the location of radio pulses (sferics) from lightning by means of the Time Of Arrival (ToA) or similar techniques (Said et al., 2010). All sensors are sensitive in the Very Low Frequency (VLF, 3–30 kHz) radio band, but differences in frequency band, sensor design, detection algorithms, sensitivity and global coverage make each network a unique instrument. Not all lightning are detected and consistently characterized and localized by all networks.

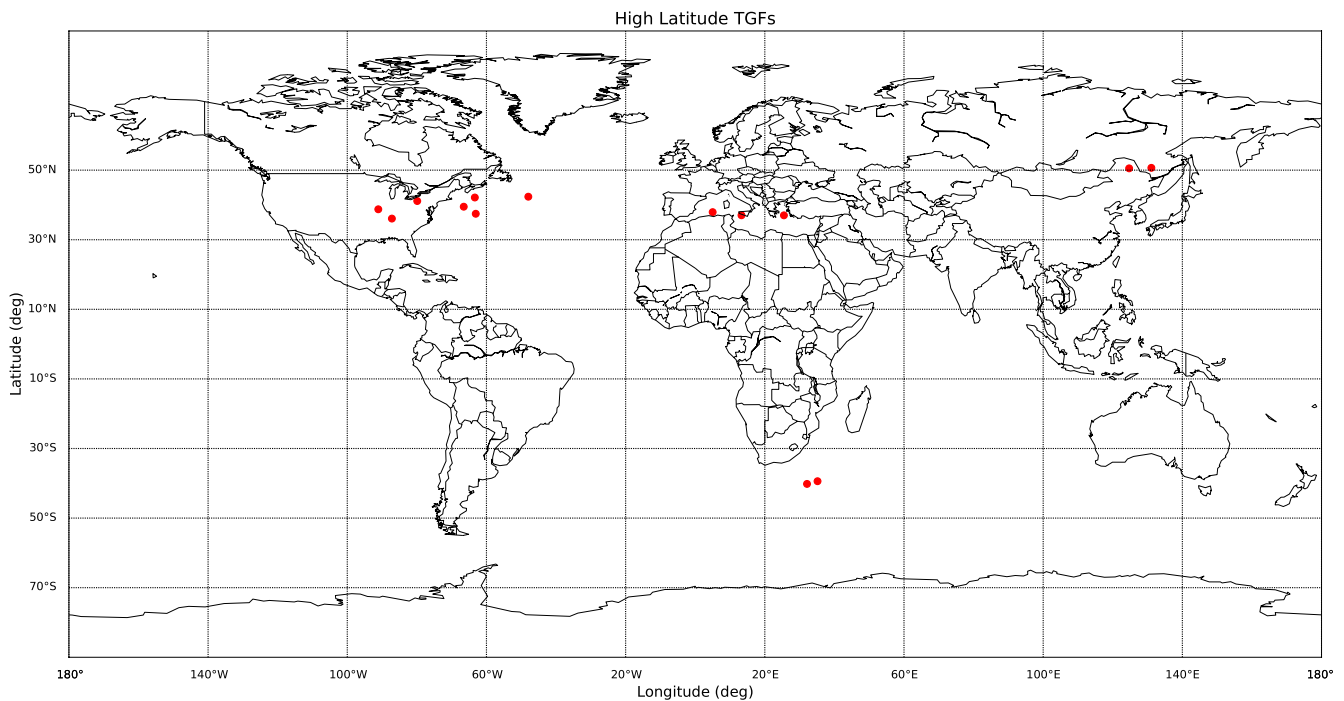


**Figure 1.** A global map of the events presented in this study (position given by Atmosphere Space Interaction Monitor's footprint at the time of detection).

ASIM has an absolute timing uncertainty of around 20–30 ms. We therefore consider a possible correlation between a TGF and a lightning stroke if it occurs within  $\pm 30$  ms from the trigger, with preference given to strokes occurring after the TGF. This is because the error on the timing is not symmetrical with respect to the event's time tag, but is more likely to have positive values. Only for the cases where MMIA data are available (nos. 1, 2 and 4) it is possible to correct the timing down to a precision sufficient to identify the associated stroke with certainty; the procedure used will be explained in Section 3.1. We also require the stroke to fall within an 800 km radius from the footprint of ASIM, since it is unlikely that TGFs can be

**Table 1**  
A Summary Table of the Mid Latitude Events Detected

Evt no.	Date and time (UT)	ISS position (lat, lon)	Duration <sup>a</sup>	BGO counts	LED counts	MMIA
1	2018-Jul-11 04:40:43	37.46, -63.07	79 $\mu$ s	58	30	yes
2	2018-Sep-19 19:26:31	37.03, 13.29	625 $\mu$ s	77	22	yes
3	2018-Oct-08 12:38:30	37.93, 5.01	56 $\mu$ s	46	-	no
4	2018-Nov-07 05:45:39	39.49, -66.53	39 $\mu$ s	51	29	yes
5	2019-Jan-30 08:14:50	-40.18, 32.13	93 $\mu$ s	106	-	no
6	2019-Jun-13 04:32:02	50.52, 124.7	26 $\mu$ s	45	-	no
7	2019-Aug-20 13:06:44	41.12, -79.89	97 $\mu$ s	80	-	no
8	2019-Aug-30 08:15:37	42.14, -63.34	39 $\mu$ s	97	-	no
9	2019-Sep-06 18:15:00	50.66, 131.09	71 $\mu$ s	142	-	no
10	2019-Nov-07 09:59:38	-39.40, 35.15	22 $\mu$ s	30	-	no
11	2019-Nov-13 03:15:44	37.01, 25.49	169 $\mu$ s	26	-	no
12	2020-Jun-30 15:38:16	38.75, -91.09	40 $\mu$ s	166	-	no
13	2020-Jun-30 15:39:22	36.08, -87.18	51 $\mu$ s	42	-	no
14	2020-Aug-16 17:41:20	42.37, -47.97	95 $\mu$ s	26	-	no

<sup>a</sup>T90.

**Table 2**  
*The Lightning Data Available for Each Event*

Evt no.	Time	$\Delta t^a$ (ms)	Location (lat, lon)	Peak current (kA)	Radio data
1	04:40:43.480	22	39.27, -65.84	-15	ENTLN
	04:40:43.478	20	38.91, -68.03	-17	GLD360
	04:40:43.480	22	39.25, -65.52	-	WWLLN
2 <sup>b</sup>	19:26:31.184	0.55	37.40, 12.93	27	ENTLN
3	12:38:30.282	2	37.22, 2.84	-36 <sup>c</sup>	ENTLN
	12:38:30.282	2	37.22, 2.88	-72	GLD360
4 <sup>d</sup>	05:45:39.997	-2	39.44, -68.79	123	ENTLN
	05:45:39.997	-2	39.55, -69.02	-24	GLD360
	05:45:40.005	6	39.55, -68.95	-	WWLLN
5	08:14:50.508	15	-40.86, 30.78	-13 <sup>c</sup>	Füllekrug, ENTLN
	08:14:50.511	18	-40.85, 30.79	-33 <sup>c</sup>	Füllekrug, ENTLN
6	-	-	-	-	not available
7	13:06:44.965	23	39.58, -80.52	19	ENTLN
	13:06:44.965	23	39.58, -80.52	18	GLD360
	13:06:44.965	23	39.57, -80.52	6	GLD360
8	08:15:37.418	16	41.57, -62.57	-25 <sup>c</sup>	ENTLN
	08:15:37.418	16	41.57, -62.56	-	WWLLN
9	18:15:00.831	18	50.89, 130.13	129	ENTLN
	18:15:00.831	18	50.83, 130.49	88	GLD360
	18:15:00.831	18	50.87, 130.10	-	WWLLN
	18:15:00.831	18	50.93, 130.06	-	WWLLN
10	09:59:38.766	-7	-38.55, 37.63	-9	ENTLN
	09:59:38.768	-4	-38.52, 37.70	84	ENTLN
	09:59:38.768	-4	-38.52, 37.70	-	WWLLN
11	03:15:44.399	14	39.28, 24.29	-23 <sup>c</sup>	ENTLN
	03:15:44.399	14	39.26, 24.29	-	WWLLN
12	15:38:17.002	3	39.36, -90.62	8	ENTLN
	15:38:17.003	4	39.37, -90.62	1	ENTLN
	15:38:17.008	10	39.36, -90.62	14	ENTLN
	15:38:17.005	6	39.37, -90.63	102	GLD360
	15:38:17.005	6	39.40, -90.63	-	WWLLN
13	15:38:17.005	6	39.38, -90.62	-	WWLLN
	15:39:22.988	7	35.29, -86.42	2	ENTLN
	15:39:22.989	7	35.29, -86.42	27	ENTLN
	15:39:22.989	7	35.29, -86.42	25	GLD360
	15:39:22.989	8	35.29, -86.41	20	GLD360
	15:39:22.989	8	35.27, -86.40	10	GLD360
	15:39:22.989	8	35.29, -86.41	-3	GLD360

*Continued*

detected at further distances (Briggs et al., 2013; Lindanger et al., 2020; Smith et al., 2016). Given the rate of WWLLN and GLD360 strokes in a 500 km radius around all ASIM TGFs, we estimate the number of strokes associated by chance in a 30 ms interval around all our 14 events to be 0.05 for WWLLN and 0.8 for GLD360.

For most events we found at least one possible associated stroke in the database of at least one of these networks. The exception is event 6, occurring in an area with low detection efficiency from any network. In other cases (nos. 1, 9, 10, 12, 13, 14), lightning activity was detected in the area, but it was not possible to select a specific stroke as the most likely associated candidate.

Radio waveforms from the candidate associated strokes were provided by ENTLN. We used them to recognize the type of lightning (intra-cloud, IC, vs. cloud-to-ground, CG) and the polarity. When MMIA data are available, the waveform is one of the references that we use to correct ASIM's timing. Table 2 provides a list of the possible associated lightning strokes with the available information. The table reports also the peak current and polarity provided by ENTLN and GLD360.

The strokes associated to event number 5 was also recorded by one of the authors during a sprite observation campaign. The instrument used is a wideband digital low-frequency radio receiver which can measure electric field strengths from around ~4 Hz to ~400 kHz (Füllekrug, 2009). The amplitude resolution is around 35  $\mu V$  and the temporal resolution is 12 ns. The receiver was placed in Klerefontein, South Africa (30.97°S, 21.98°E).

Finally, the Lightning Imaging Sensor (LIS) on the ISS (Blakeslee et al., 2020) was used in event no. 2 to correct ASIM's time, by aligning the pulses detected by LIS and MMIA, taking into account the instrumental differences. ISS/LIS records in the 777.4 nm band and is also nadir-pointing as MMIA, allowing direct comparison after converting the intensity to the same units. The accuracy of this time correction is around 2 ms. LIS was only used for event no. 2, as in that particular case it further enhanced the precision of the time correction. There are no LIS data available for events 1 and 4 and in the cases without MMIA data LIS does not add any useful information for this study, since it does not provide neither waveforms nor peak current values.

### 2.3. Meteorological Data

The Cloud Top Temperature (CTT) was used to evaluate the severity of the TGF-producing storms and compare their characteristics to the low-latitude ones. Images of CTT were obtained, using the French database ICARE, from the appropriate geostationary satellites: Meteosat, GOES or Himawari. A CTT image is provided every 10 min for GOES, 15 min for Meteosat and 20 min for Himawari. The image closer to the timestamp of the TGF was used.

The global lightning flash rate is obtained from the LIS/OTD climatology database (Albrecht et al., 2016). The maps offer the monthly flash density per square kilometer over the globe with a resolution of 0.5° in both latitude and longitude. This is used in the estimate of the TGF-to-lightning ratio, with the final goal of comparing the ratio at mid latitude with the one at low latitude. We point out that we do not perform a direct

**Table 2**  
Continued

Evt no.	Time	$\Delta t^a$ (ms)	Location (lat, lon)	Peak current (kA)	Radio data
14	17:41:20.153	17	40.48, -53.72	95	ENTLN
	17:41:20.153	17	40.43, -53.72	178	GLD360
	17:41:20.153	17	40.40, -53.73	-	WWLLN
	17:41:20.153	17	40.48, -53.72	-	WWLLN

*Note.* When a timing correction was available, the time difference from the stroke is calculated with respect to the corrected TGF time.

<sup>a</sup>Stroke time-TGF time. <sup>b</sup>Case with absolute timing after LIS correction.

<sup>c</sup>The subsequent analysis of the waveform reclassified the event as +IC.

<sup>d</sup>Case with absolute timing after MMIA correction.

comparison between ASIM data and the LIS/OTD maps, as the latter are made from observations in the period 1995–2014.

Atmospheric pressure and temperature at tropopause level are taken from the NCEP/NCAR atmospheric reanalysis (Kalnay et al., 1996). Pressure is needed to calculate the atmospheric transmission factor in the column of air above the thundercloud, which is assumed to have the greatest impact on the detection of TGFs at mid latitudes. The temperature of the tropopause is a proxy for its altitude and can be compared with the minimum CTT to find evidence of deep convection. All data are given on monthly maps with a grid size of  $2.5^\circ \times 2.5^\circ$  and are long-term mean values calculated over the period 1981–2010.

### 3. Methods

Because mid latitude TGFs are being observed for the first time, and because we have a solid amount of auxiliary data, each event in our list is analyzed separately. A few notable cases are discussed in detail in Section 4. For all the others, we point the reader to the Supporting Information S1, where TGF lightcurves and CTT images are provided.

#### 3.1. Stroke Correlation and Time Correction

As mentioned in Section 2.1, ASIM has an absolute timing uncertainty of about 20 ms. This can be minimized by aligning light pulses detected by MMIA with the corresponding strokes from ground networks, under the assumption that many of the lightning sferics detected within the MMIA field of view show up as peaks in the photometers light curves. Since the relative time accuracy between MXGS and MMIA is below 80  $\mu$ s, correcting the MMIA time means correcting the MXGS timing too, which in turn means that we can have a much more accurate timestamp for those TGFs which have MMIA data (we remind that MMIA is only active at night). This is the case for three events (numbers 1, 2 and 4), although for event no. 1 it was actually not possible to find the correct alignment between MMIA and ground-based lightning detection networks. In this case, the issue was due to the associated stroke being outside the field of view of the MMIA, which is significantly smaller than the one of MXGS.

It was possible to improve the absolute timing accuracy of two events, nos. 2 and 4. For event 2, the MMIA data were aligned with both GLD360 and LIS data, shifting the time by 10 ms. The LIS-based correction was found to be better than the one based on ground networks, as it was not possible for this event to univocally align the set of ground-detected strokes with the pulses in MMIA. As a result one of the candidate stroke was found to occur 552  $\mu$ s after the TGF. This cannot strictly be considered a simultaneous association as defined by Connaughton et al. (2013), as they require the stroke to be no more than  $\pm 200 \mu$ s from the TGF to consider it as the associated stroke, but it is enough for our purposes. For event 4 the alignment was done with GLD360 detections and the shift amounted to 7.6 ms. However, the closest stroke ended up being 2 ms before the TGF, and therefore cannot be considered as a simultaneous association. For all other events, when we have several strokes within 30 ms of the TGF and in the field of view of ASIM, we are not able to determine which one is the associated stroke, but we keep all of them as candidates. Event 6 is the only one without any candidates. The exact location of the stroke is needed for the atmospheric temperature analysis in Section 5.1. For the events with ambiguous correlation we used the average location of all candidates, since they were all coming from the same active core. We did the same for event no. 6, using the lightning core that was active during the same second in which the TGF occurred.

#### 3.2. Exposure Time

In order to estimate the TL<sub>Rat</sub> mid latitudes we need to know ASIM's exposure time; with that term we refer to the amount of time in seconds during which a certain geographic location is within the Field of View (FoV) of ASIM. We consider a circular FoV for MXGS with a 500 km radius centered at the sub-satellite point. This particular distance was chosen as most TGF are detected within such radius; see Figure 3 in

Smith et al. (2016), Figure 8 in Briggs et al. (2013) and Figure 3 in Lindanger et al. (2020). The equivalent analysis for ASIM is still unpublished but points in the same direction. This 500 km distance is intended as an average radius that separates an inner region with approximately uniform probability of detecting a TGF and an outer region in which detections are extremely rare. We note that this radius is different than the 800 km one that we introduced in Section 2.2 because, according to the figures mentioned, detection of TGFs from more than 500 km away are possible, but rare enough to not have an impact on the exposure.

The exposure time is longest at the highest latitudes reached by the ISS because of the orbital geometry. However, at high latitude there is a stronger background of ionizing radiation coming from Earth's radiation belts, which is automatically reduced by decimation, a process in which a pre-determined number of counts within a time frame is automatically rejected, to prevent overloading of the MXGS read-out buffer. It is significant only over northern Canada and Southern Australia, but it has impact on both the trigger logic and the detection of TGFs. As a consequence, we have no way of determining if it caused any missing detections and cannot calculate a TLR for those regions. The same applies to the regions at the border of the SAA, where MXGS is automatically turned off. The SAA is implemented for ASIM as a fixed, rectangular area. The exact values of the borders have been changed a few times since commissioning, starting from a rectangle between  $-5^{\circ}$ – $-60^{\circ}$  in latitude and  $-80^{\circ}$ – $+40^{\circ}$  in longitude until December 2018. The latitude borders were never changed, but the longitude span was reduced gradually from the initial  $+40^{\circ}$ – $0^{\circ}$  in steps of  $10^{\circ}$  between December 2018 and February 2019.

We used housekeeping data to keep track of when MXGS was on and when it was off. We then coupled this information with the position, obtained by tracking the orbit of the ISS, with a  $0.5^{\circ}$  resolution in both latitude and longitude. The distance between ASIM's footpoint and the center of a map bin is calculated. If it's less than 500 km the bin is entirely included, otherwise it is entirely excluded; we do not consider fractional bins. The group of all the included bins around the footpoint is the field of view of MXGS at that particular instant. The exposure maps were computed on a monthly basis and then combined with the LIS/OTD lightning climatology maps. We chose the monthly climatology maps to account for concurrent time variability of lightning flash density and of ASIM's exposure, the latter being especially evident in equatorial Africa due to the subsequent reductions of the SAA exclusion region.

### 3.3. TGF-to-Lightning Ratio

Once the exposure was calculated we were able to calculate the observed TLR. TLR is the base for estimating the rarity of TGFs at mid latitude but it is an interesting value in itself, as it is known to be dependent on the geographical area. The differences in the values for the equatorial regions are discussed in Fabr6 et al. (2019). If atmospheric absorption is the reason why we see so few TGFs at mid latitude the TLR there would be similar to one of the equatorial values, when the lower detection efficiency due to a higher atmospheric absorption is properly accounted for. In terms of procedure, it means that we can estimate the TLR at mid latitude by scaling the equatorial sample of TGFs from ASIM for the atmospheric absorption factor of the mid latitudes. The TLR obtained this way is expected to be compatible with the actual observations that are the subject of this paper. The full procedure is detailed in the following.

The number of lightning flashes that occurred inside the FoV of MXGS is obtained as the product between lightning flash density and exposure time, according to Equation 1.

$$F_{ij}^{(m)} = \frac{1}{86400} E_{ij}^{(m)} L_{ij}^{(m)} dS_j \quad (1)$$

where  $(m)$  corresponds to the month of the year,  $i$  and  $j$  are the index of the longitude and latitude bins, respectively. Calculations are carried out on a grid with  $0.5^{\circ} \times 0.5^{\circ}$  bin, with longitude in the  $[-180^{\circ}, +180^{\circ}]$  interval and latitude in the  $[-80^{\circ}, +80^{\circ}]$  interval.  $L_{ij}^{(m)}$  is the LIS/OTD average lightning flash density during month  $(m)$  expressed as flashes/( $\text{km}^2\text{day}$ ),  $E_{ij}^{(m)}$  is the exposure time during month  $(m)$  in seconds / bin, 86,400 is the number of seconds in a day,  $dS_j$  is the bin surface element in  $\text{km}^2$ . The bin surface element depends on latitude and is approximated as  $dS_j = \cos(\phi_j)3098\text{km}^2$ , with  $\phi_j$  latitude corresponding to bin  $j$ .

Figure 2 shows the three steps of the process for the month of July 2019: The top panel is the lightning flash density from the LIS/OTD maps; the middle panel shows ASIM's exposure time; the lowest panel

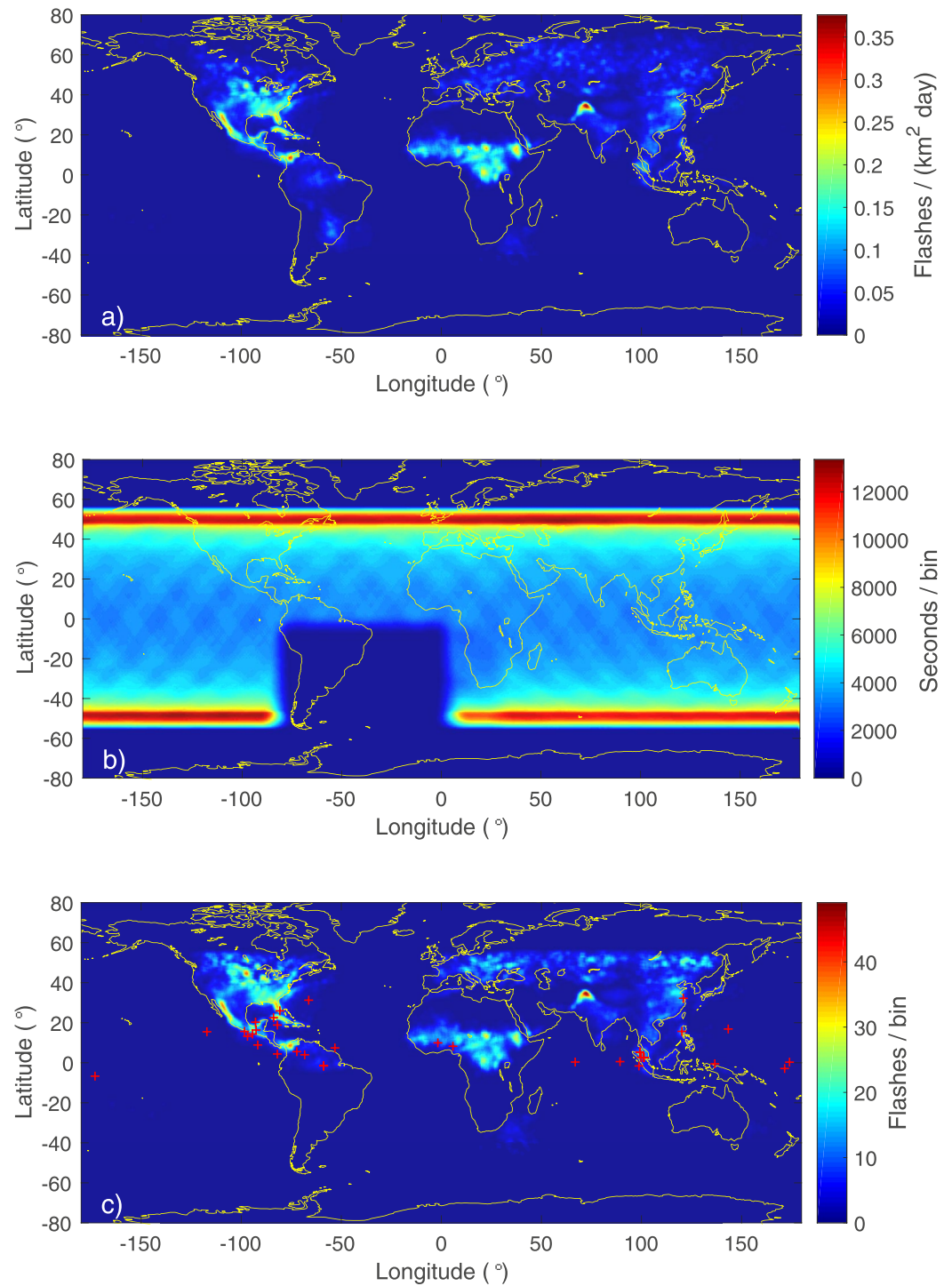


**Figure 2.** (a) Global lightning flash density, from Lightning Imaging Sensor/OTD global climatology maps. (b) Atmosphere Space Interaction Monitor's exposure, with the South Atlantic Anomaly very visible. (c)  $F_{ij}^{(m)}$ , as defined in the main text, with the Terrestrial Gamma-ray Flashes detected in the corresponding period (red crosses). Here we show the month of July, 2019 as an example. Bin size in all maps is  $0.5^\circ \times 0.5^\circ$ .

shows  $F_{ij}^{(m)}$ , with detected events superimposed. The calculation was done on a monthly basis and then the monthly maps (panel c in Figure 2) were summed to obtain seasonal maps and the map for the full period of interest  $F_{ij}$ , calculated according to Equation 2.

$$F_{ij} = \sum_m F_{ij}^{(m)} \quad (2)$$

This final product  $F_{ij}$  represents an estimate of the distribution of total number of lightning flashes, potentially associated to TGFs detected by ASIM at any given position and for the total period of interest.

We defined two different TLRs: the regional average TLR and the peak TLR. We now detail the steps used to calculate each of them.

Regional average TLR:

1. Definition of the Regions of Interest (ROI). In this work we consider seven ROIs: three at low latitude and four at mid latitude (see Figure 5) At low latitude, they correspond to the classic lightning hotspots and are used both for the comparison with previous results and as a reference for comparison to the mid latitude regions. At mid latitude they are built around the four regions where we have detections.
2. Integration of the combined exposure-lightning density maps over the ROI.
3. The regional average TLR is calculated as the ratio between the number of TGFs  $N_T$  observed within a ROI and the number of exposure-corrected lightning flashes in the same area.

Peak TLR:

1. TLR is computed as before but for smaller regions of  $10 \times 10$  square degrees centered at each grid point ( $0.5^\circ \times 0.5^\circ$  resolution).
2. The obtained TLR is considered valid only if the number of TGFs in the area is greater than 10, to reduce the statistical fluctuations. This actually excludes all mid latitude regions, which were treated differently.
3. The maximum TLR computed in this way are stored for each ROI and will be referred to as peak TLR in the following.

At this point we need to verify if the limited number of detection that we have at mid latitudes is comparable with the same TLR observed in equatorial regions, scaled for the higher atmospheric absorption. We assume that the intrinsic intensity distribution of TGF is self-similar at all latitudes, because at this point we have no theoretical or empirical reasons to believe otherwise. This assumption is consistent with observations according to the results presented in Section 4. We then estimate the TGF production rate at mid latitudes by taking the equatorial sample, scaling its count distribution by the relative transmission coefficient and counting the number of TGFs that would still be above the detection threshold; this latter number will be compared with the actual observations. The process is detailed in the following.

1. The long-term monthly mean values of the atmospheric pressure at tropopause level are obtained from the NCEP/NCAR reanalysis. From this we calculate the column density and transmission factor for gamma photons, using the equations and coefficients presented in Smith et al. (2010). For the column density above the tropopause  $\Sigma$ , expressed in  $\text{g cm}^{-2}$ :

$$\Sigma = 1.04173P + 5.17 \quad (3)$$

where P is the atmospheric pressure (hPa) at the tropopause and the numeric coefficients were derived from the U.S. Standard Atmosphere and from (Humphreys, 1964). For the transmission factor  $\alpha$ :

$$\alpha = e^{-\Sigma/45} \quad (4)$$

where the folding length of  $45 \text{ g cm}^{-2}$  was derived by Monte Carlo models in Smith et al. (2010). This equation was developed using the average RREA spectrum to simulate a TGF, and therefore implicitly includes the dependence of the transmission factor on the energy of the photon. The transmission factor represents the fraction of photons that, from that altitude, traverse the whole layer of atmosphere and reach the detector.

2. We then calculate in each map bin the relative transmission factor with respect to lightning hotspots. This is the ratio between the monthly maximum  $\alpha_{max}$  and  $\alpha$  in the considered bin, and is the value by which the TGFs intensity distribution at low latitudes will be scaled, under the assumption that the intrinsic intensity distribution holds at all latitudes. We use the number of counts of the TGFs as a proxy

Fraction of TGFs above threshold

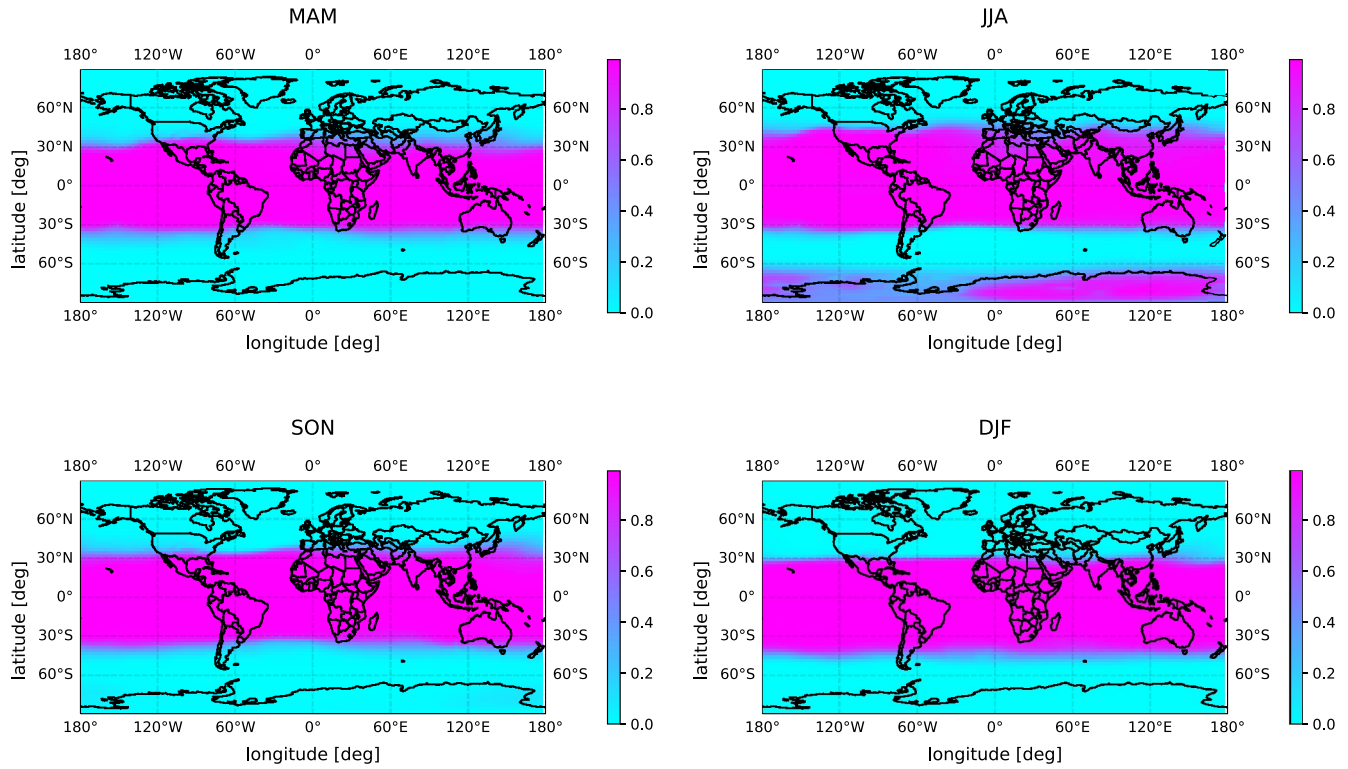


**Figure 3.** The fraction of Terrestrial Gamma-ray Flashes above detection threshold mapped on the globe, for each season of the year.

for intensity, so our source intensity distribution is the number of counts distribution of the equatorial sample, which consists of all TGFs detected between  $+15^\circ$  and  $-15^\circ$  of latitude. The value of  $\alpha_{max}$  is uniform in the equatorial band and represents a typical value for the equatorial ROIs. It is important to note that we scale the intensity distribution because attenuation acts on single photons, meaning that it reduces the intensity of every single TGF, not the number of detected TGFs itself.

3. After the intensity distribution is scaled we estimate the fraction  $\chi$  of events that are still above the trigger threshold. The thresholds that we used are the actual values, recovered from ASIM's housekeeping files, and range from 10 to 17 counts in the  $300 \mu s$  trigger window.
4. The  $\chi$  factor is calculated on the global map and multiplied bin-by-bin with the combined lightning and exposure maps, to obtain an estimate of the number of TGF occurring in each area of the globe. We call the result of this product effective lightning number  $F^{eff}$ , the number of lightning potentially associated to a TGF detected by MXGS accounting for the local conditions at the tropopause, calculated according to Equation 5:

$$F_{hk}^{eff} = \sum_m \chi_{hk}^{(m)} F_{hk}^{(m)} \quad (5)$$

where  $h$  and  $k$  are the index of the longitude and latitude bins, respectively (calculations are carried out on a grid with  $2.5^\circ \times 2.5^\circ$  bin, dictated by the NCEP/NCAR reanalysis bin size),  $F_{hk}^{(m)}$  is the monthly exposure-corrected lightning flash density calculated according to Equation 1 and rebinned to the new bin size,  $\chi_{hk}^{(m)}$  is the monthly absorption correction factor defined above, and the sum is carried out over the full period of interest.

Figure 3 shows the seasonal variation of  $\chi$  on the global map and shows a very steep transition from tropical to temperate latitudes, in correspondence with our mid latitude ROI. This is the reason why an average value of the TLR in the mid latitude regions would not be representative of the actual values.

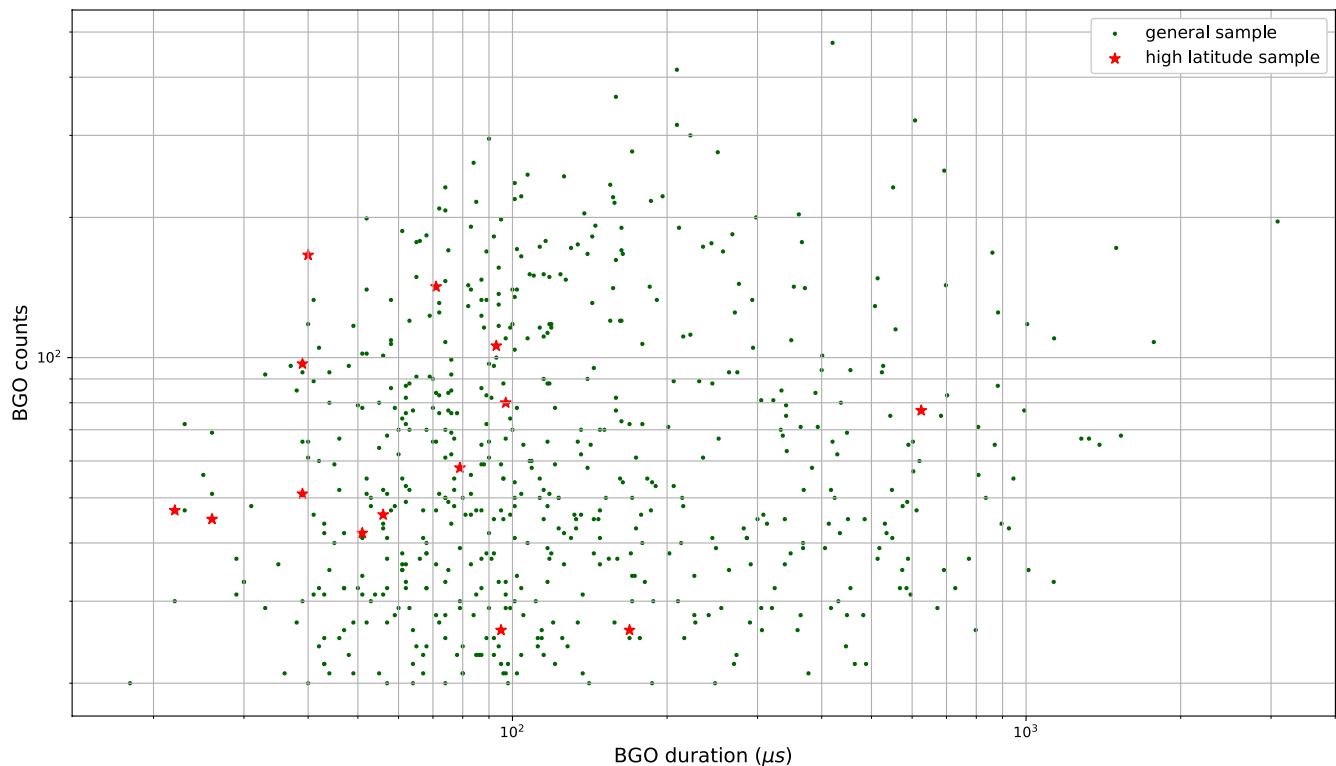


**Figure 4.** The number of counts and duration (in the high energy detector) of the mid latitude Terrestrial Gamma-ray Flashess compared with Atmosphere Space Interaction Monitor's general sample. Multi-pulse events are excluded from the sample. The number of counts is not corrected for instrumental effects.

Under the assumption that the number  $x$  of observed TGFs is the result of a Poisson process with expected value  $\theta$ , we calculate the 68% and 95% confidence intervals  $[\theta_L, \theta_U]$  for the number of TGFs in the mid latitude ROIs according to Equation 6 (Johnson et al., 2005).

$$\theta_L = 0.5\chi_{2x, \alpha/2}^2, \quad \theta_U = 0.5\chi_{2(x+1), 1-\alpha/2}^2 \quad (6)$$

where  $\chi_{n,p}^2$  is the quantile function corresponding to probability  $p$  of a  $\chi^2$  distribution with  $n$  degrees of freedom, and  $\alpha = 0.32$  or  $0.05$  for 68% and 95% confidence intervals respectively. We divide these confidence intervals by the effective lightning number to estimate the range of TLR values in the mid latitude ROIs. We then compare these ranges to the average and peak TLR measured in the low-latitude ROIs. The assumption of a Poisson process corresponds to assuming that the observed number of TGFs is the result of a large number of realizations given by the exposure-corrected number of lightning, each with a constant and small probability of producing a detectable TGF given by the TLR. We understand this assumption is quite crude, given the fact that it does not account for the different lightning and local electric field characteristics which definitely play a role in the TGF production process. However, we consider this assumption as acceptable when one is discussing an average quantity such as the TLR.

### 3.4. Thunderstorm Environment

We analyze the thunderstorm environment with data from geostationary satellites (see Section 2.3). The aim is to have an overview of the evolution of the storm up to the production of the TGF, and of the CTT. CTT is used as a proxy for cloud top altitude (in the troposphere, lower CTT implies higher altitude), since a more precise conversion between the two requires a detailed model of the local atmosphere. Additional information on the storm severity was obtained by tracing the flash activity recorded by the ENTLN, WWLLN and GLD360 lightning detection networks.

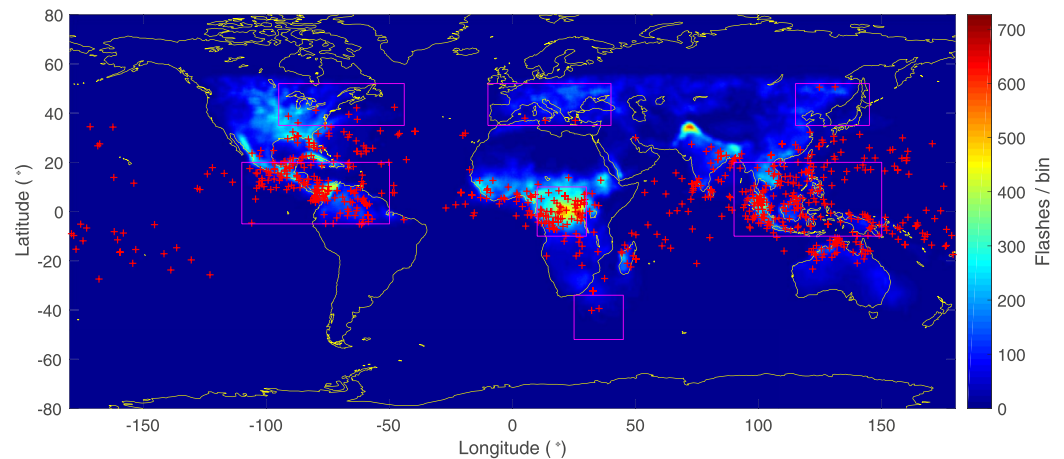


**Figure 5.** Exposure-corrected lightning flash density  $F_{ij}$  for the full period of interest. Superimposed are the Terrestrial Gamma-ray Flashes (TGFs) detected in the same period (red pluses) and the regions of high TGF production (pink boxes).

#### 4. Results

Figure 4 shows the duration and the number of counts, for both the global ASIM data set and the mid latitude subset. A two-sample Kolmogorov-Smirnov (KS) test on the number of counts distribution for the mid latitude sample and the global TGF sample results in the non-rejection of the null hypothesis that the two samples are drawn from the same distribution. However, the same test applied to the duration ( $T_{90}$ ) distributions indicates that the null hypothesis can be rejected at a 5% significance level, suggesting that the duration distribution of the mid latitude TGFs is significantly different from that of the global sample. The global sample used for this test includes all the ASIM TGFs detected during the reference period considered for the analysis, except all multi-peak TGFs and the mid latitude sample.

Despite the long duration, event no. 2 is not a terrestrial electron beam, as those are at least 2 ms long, and even more at high latitudes due to the longer field lines. Moreover, there is a strong association with a local stroke and no matching lightning activity at either magnetic footpoint (north and south).

Figure 5 shows the combined exposure and lightning maps covering the whole period of analysis, with the ASIM TGFs superimposed. Figure 6 is the same map for each season. Some areas have high lightning activity all year round, while others activate on certain periods only. This is especially true at the latitudes we are interested in, as there we have stronger seasonal variability.

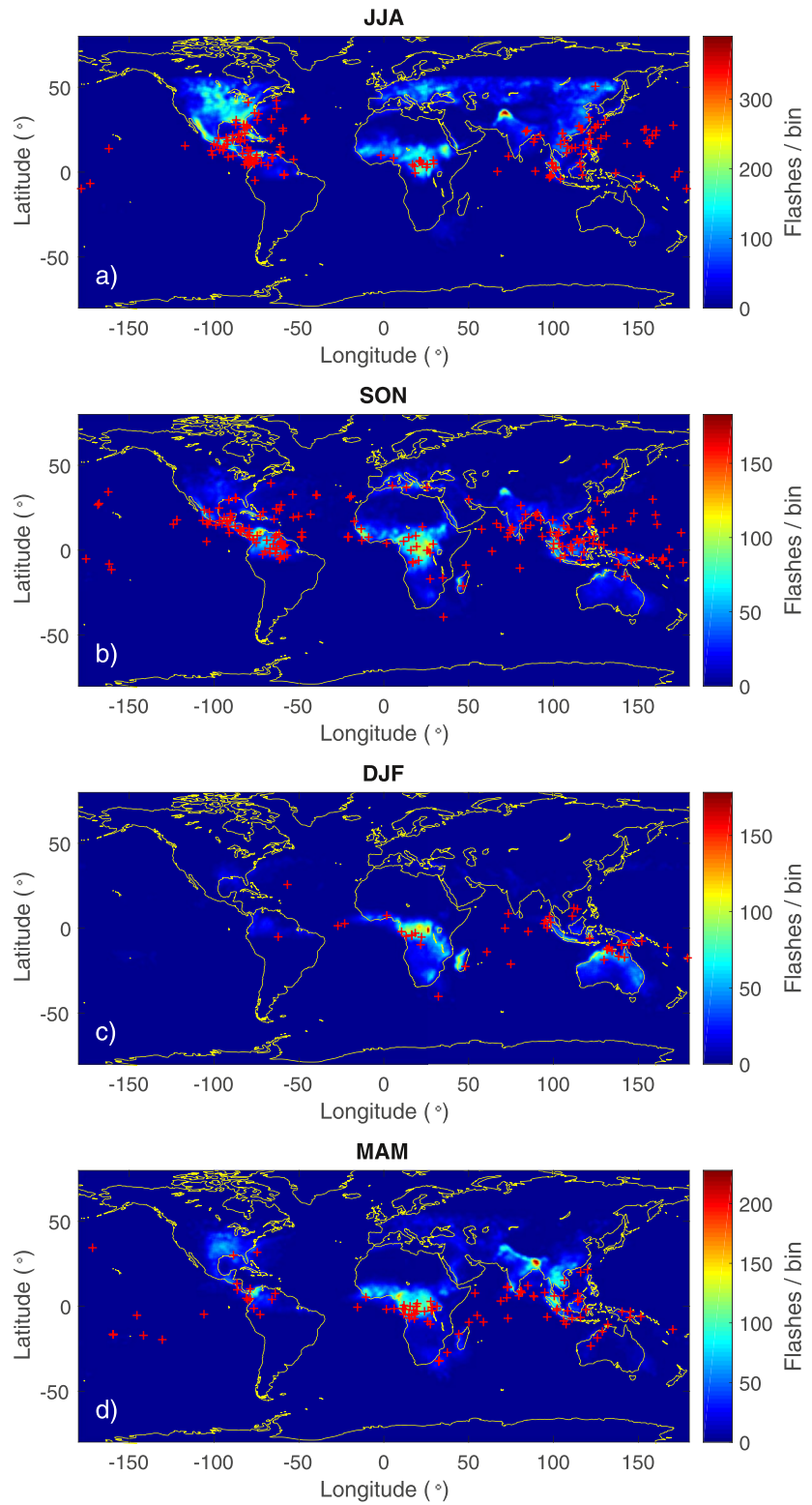
We also see that there are regions of relatively low lightning activity, which nonetheless regularly produce TGFs and regions where a high lightning activity does not lead to TGF production. Examples of the former are the Pacific Ocean and the South African ROI, while of the latter are the north-western Himalayas, central USA and California.

We now present three case studies of particular interest. Event number 4 was chosen for the accompanying, high-quality data from MMIA, that allowed a correction of the absolute timing accuracy down to about 100  $\mu$ s; event number 5 because its parent stroke was independently recorded by one of the authors; event number 9 because it's the northernmost of the sample.

##### 4.1. Event No. 4: November 7th, 2018

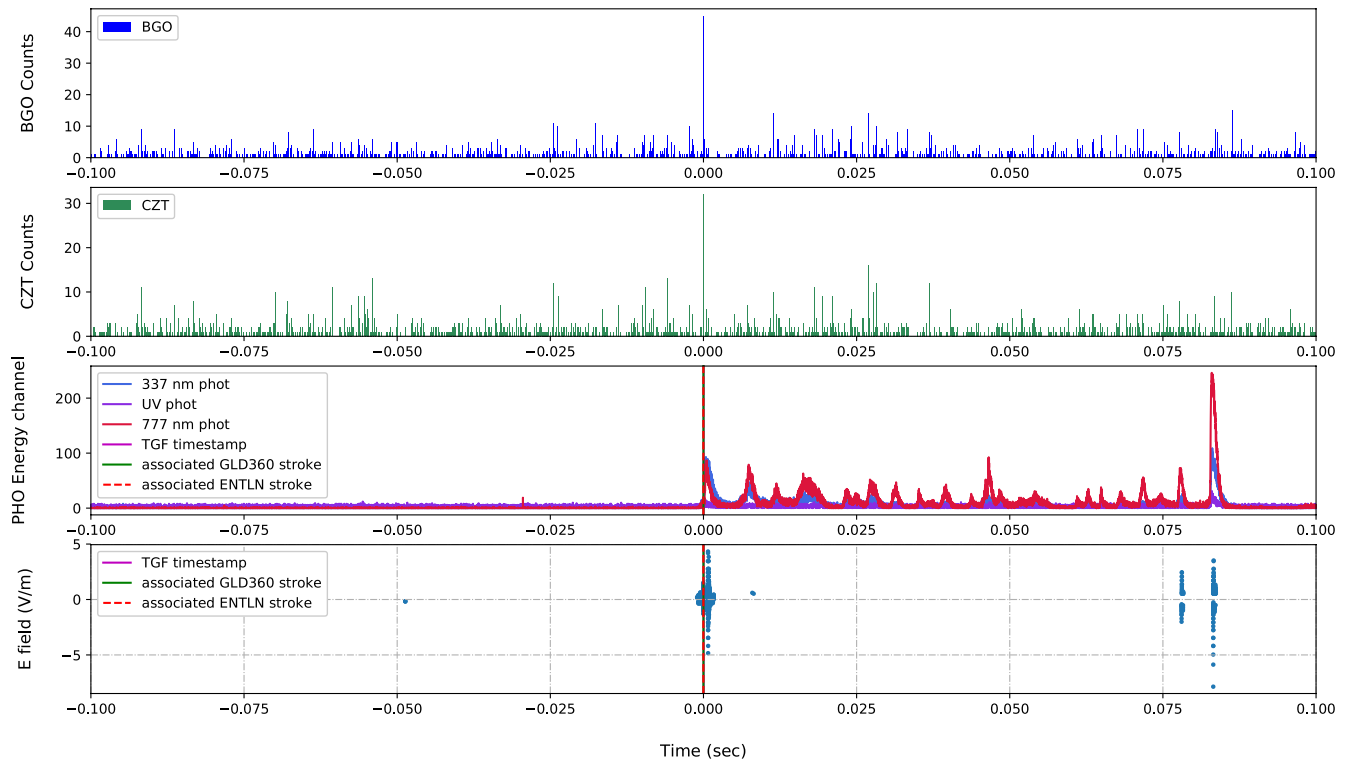
The event occurred on November 7th, 2018 at 05:45:39 UTC over the northern Atlantic Ocean, almost 800 km away from the North American coast. MMIA and LED were active at the time, and both recorded data related to the TGF.

Figure 7 shows all these data synchronized between the different instruments and centered around the associated stroke, as recorded by GLD360. MMIA data have been shifted to agree with the sequence of



**Figure 6.** Seasonal variations of the combined exposure and lightning activity, with Terrestrial Gamma-ray Flashes superimposed.

2018-11-07 05:45:39.997317632



**Figure 7.** The Bismuth-Germanium Oxide (High Energy Detector (HED)), CZT (Low Energy Detector (LED)), optical and radio data for the event of 2018-Nov-07. The bin size for HED and LED histograms is 100  $\mu$ s.

strokes detected by GLD360, therefore correcting ASIM's absolute timing uncertainty as described in Section 3.1; MXGS data were also shifted accordingly. For this event the MXGS-MMIA relative timing accuracy is  $\pm 80 \mu$ s. Figure 8 is a zoom in around the correlating stroke, to better show the relative position of the TGF and the MMIA optical pulse, and the stepping leader activity in the radio band (the isolated spikes in the waveform on the left of the main stroke). ENTLN reported a stroke which is compatible in position and with a timestamp 30  $\mu$ s earlier than the GLD360 one; this stroke is also shown in Figure 8. The two strokes align almost perfectly on the waveform, after accounting for the propagation time to the detector, therefore suggesting that they are two reconstruction of the same current pulse. The flash could have been extended and branched, leading to the difference in detection and reconstruction. It is also worth noting that both network automatically classified the flash as CG, and only the inspection of the waveform proved otherwise. The stroke is likely an IC lightning, mainly because of the lack of detected radio activity before the TGF-associated pulse and the short timescale of the structures in the pulse itself. It is also possible that the stroke started as an IC channel and subsequently connected to the ground. The peak current of this stroke is  $123 \pm 49$  kA, obtained from post-processing of ENTLN waveform data. The positive sign of the current indicates negative charge being accelerated upwards. GLD360 instead reported a peak current of  $-24$  kA, but with the data in our possession we cannot further investigate the discrepancy. This event presents as a typical ASIM TGF, occurring at the onset of a pulse in radiation detected in the 337 and 777.4 nm bands and after a period of no optical activity (Heumesser et al., 2021). A very slow rise in luminosity before the TGF and the proper pulse is also visible, especially in the 337 nm band: this has been noticed in many of the events where MMIA data are available and is interpreted as signal from the lightning leader channel developing upwards (Østgaard, Balling et al., 2019; Østgaard, Neubert et al., 2019).

The storm, shown in Figure 9, is a big system of cells organized in a line, slowly moving toward north-east. The convective regions inside each cell are small and relatively weak, with a minimum CTT of  $-67^\circ\text{C}$ . The

2018-11-07 05:45:39.997317632

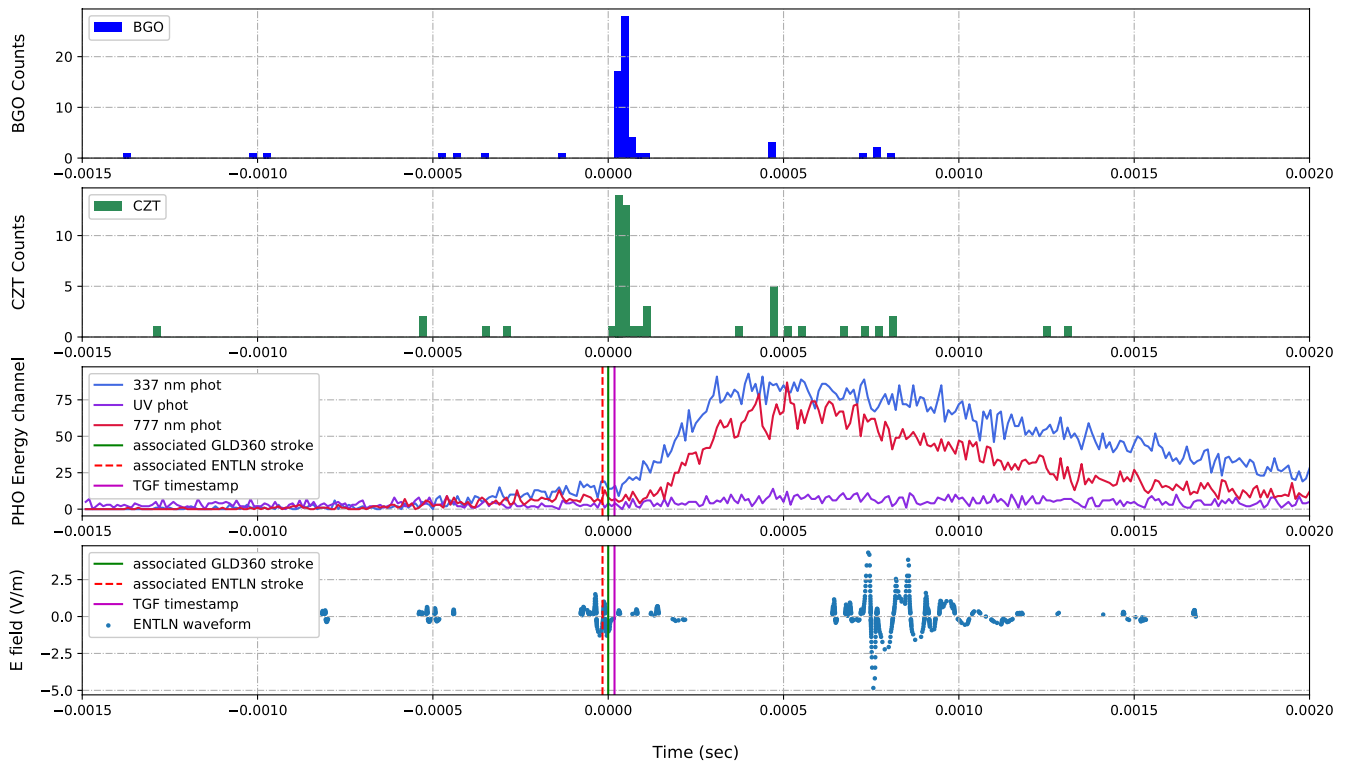


**Figure 8.** A zoom in of Figure 7 around the associated strokes, with leader stepping visible. The bin size for High Energy Detector and Low Energy Detector histograms is 20  $\mu$ s.

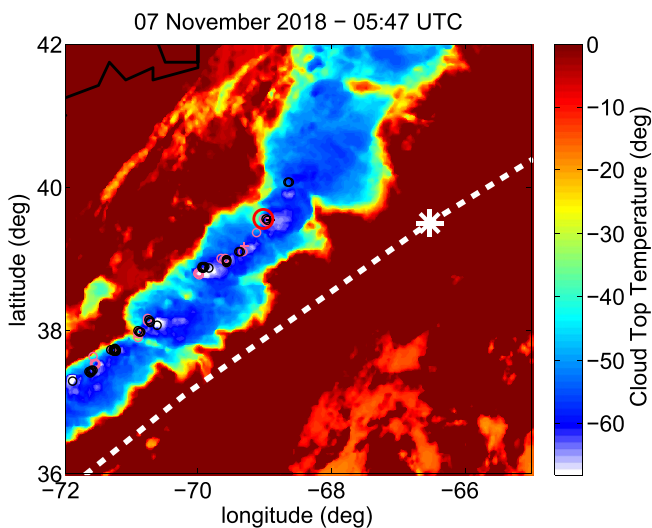


**Figure 9.** The storm system for Terrestrial Gamma-ray Flashes (TGF) number 4. The circles and the pluses are -CG and +CG respectively, detected within 5 min around the TGF (the pink before and the black ones after). The red circle is the associated stroke. The dashed line shows the International Space Station trajectory and the white star marks its position at the time of the detection.

cell that produced the TGF was a warmer ( $-53^{\circ}\text{C}$  at TGF position) and newly developed one, which seemed from the satellite images to have just reached its maximum vertical development. The stroke that produced the TGF was located within a cloud region with a much less cold top ( $-53^{\circ}$ ).

The west part of the northern Atlantic Ocean is well known for TGF occurrence: events from this area are included in RHESSI's catalog (Smith et al., 2010) and are often seen by ASIM. The mid latitude events list includes seven from this ROI, three of which actually over U.S. mainland.

#### 4.2. Event No. 5: January 30th, 2019

This event happened on January 30th, 2019 at 08:14:50 UTC over the ocean south-east of South Africa. Because it was daytime, neither MMIA nor LED were operative, and therefore we only have the HED data. ASIM's footprint was at  $-40^{\circ}$  of latitude.

ENTLN was the only one to detect two candidate parent strokes, less than 10 ms apart. These strokes are both part of the same IC flash (Figure 10) and are associated with the initial breakdown and the final continuing current respectively. The ENTLN sensors also recorded the radio wave produced by the flash. The signal was also serendipitously detected by one of the authors (Füllekrug) during a sprite detection campaign in South Africa; this recording is also shown in the figure. As in the previous event, the waveform has the typical shape of an IC flash, with leader

2019-01-30 08:14:50.510874271

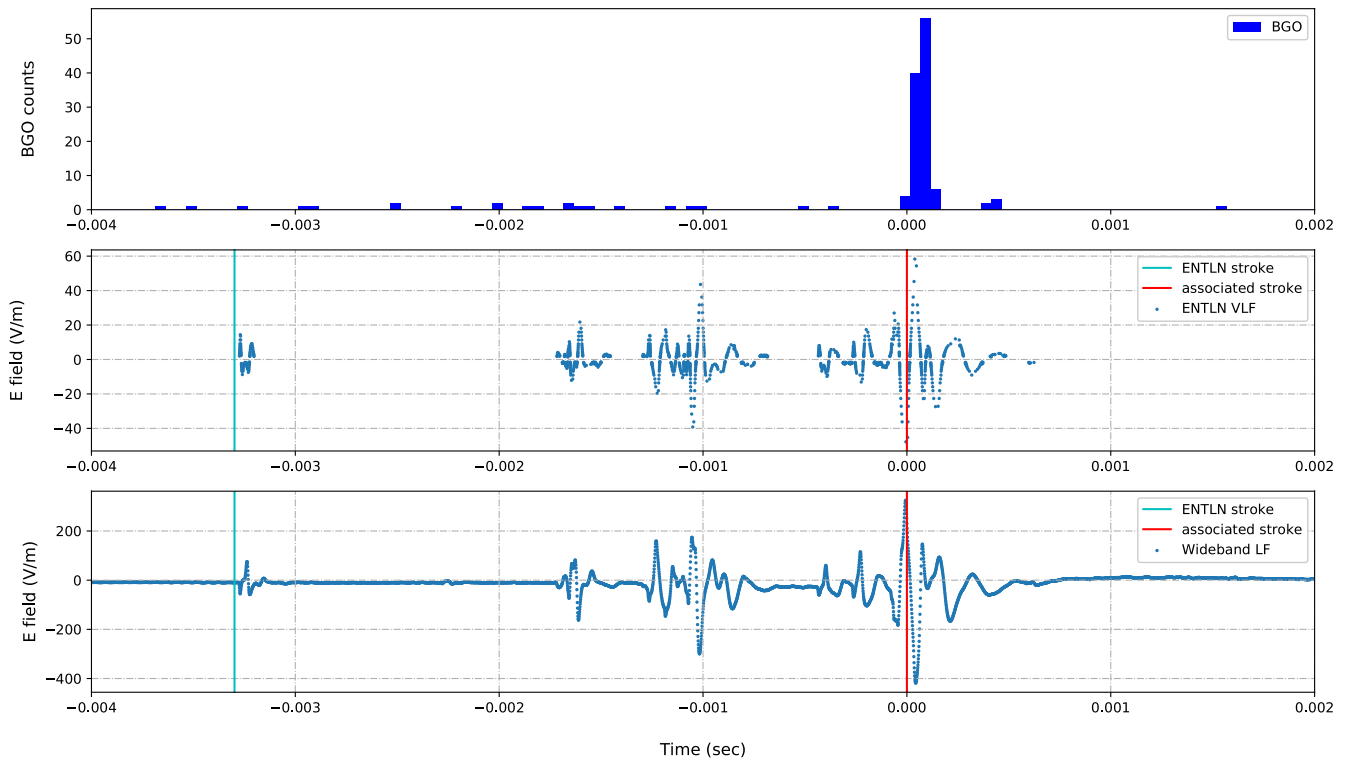


**Figure 10.** Top: the Bismuth-Germanium Oxide lightcurve, with a bin size of 50  $\mu$ s. Middle: the radio waveform recorded by Earth Networks Total Lightning Network for the associated stroke. Bottom: the radio waveform as recorded by the authors (Füllekrug). Here the Terrestrial Gamma-ray Flashes is matched to the second sferic based on the largest peak current (see main text).

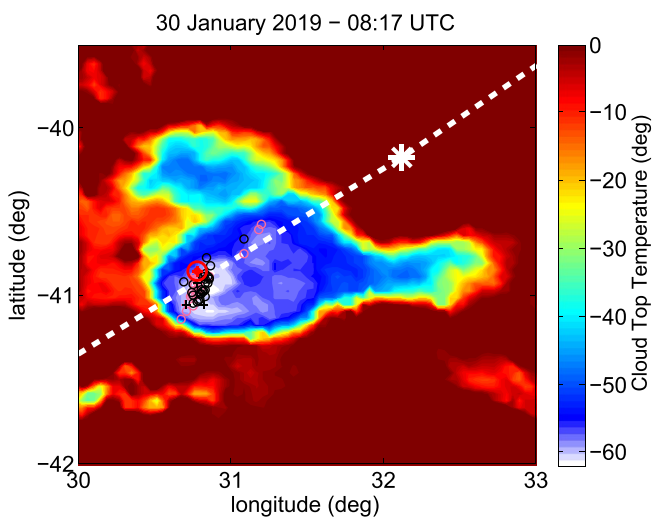


**Figure 11.** The storm environment for event number 5. The circles and the pluses are the -CG and +CG strokes, respectively, detected within 5 min around the Terrestrial Gamma-ray Flashes (the pink before and the black after). The red symbols mark the two associated strokes. The dashed line shows the International Space Station trajectory and the white star marks its position at the time of the detection.

stepping clearly visible. Due to the lack of optical data, we cannot improve ASIM's timing precision for this event as described in Section 3.1, therefore we cannot determine which radio pulse is actually associated with the TGF. We consider the later stroke to be more likely because of the higher peak current and Figure 10 was produced accordingly, but we stress the fact that ASIM's absolute timing for this event does not allow for a reliable association. Although the association to a specific stroke is questionable, the location the TGF is coming from is fairly clear, given the compact nature of the stroke and of the lightning activity recorded around the TGF time, as described below.

The storm (Figure 11) was a single cell, compact and fairly isolated. The storm activity developed on January 29th inland and decayed during the night, while moving over the ocean and away from the coast. In the morning of the 30th the TGF-producing cell intensified and produced the TGF during this second growing phase. The TGF occurred at the periphery of the coldest core of the cell, in a region with a temperature of  $-57^{\circ}\text{C}$ . The absolute minimum temperature,  $-62.5^{\circ}\text{C}$ , was reached half an hour later and corresponded to a maximum in lightning activity. Temperatures in this range indicate a strong but not severe storm.

It is worth noting that the LIS/OTD map presented in Figure 5 shows a hotspot of lightning activity east of South Africa, which extends from

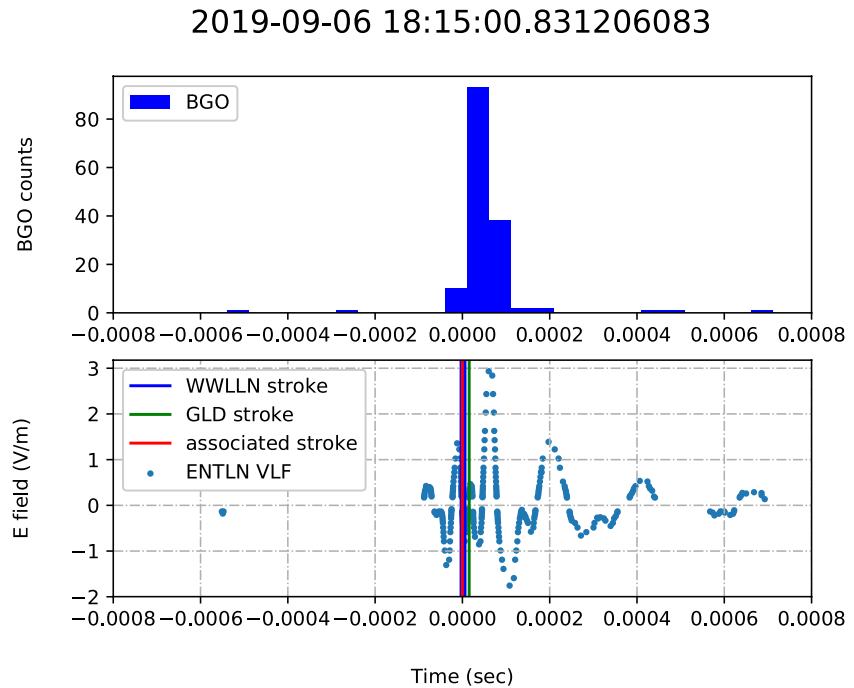


**Figure 12.** The Bismuth-Germanium Oxide lightcurve, with a bin size of  $50\mu s$  (top) and the waveform recorded by Earth Networks Total Lightning Network for the candidate parent stroke (bottom).

Madagascar down to the latitude of this event; ASIM has also detected other TGFs from this region, although only another one so far south.

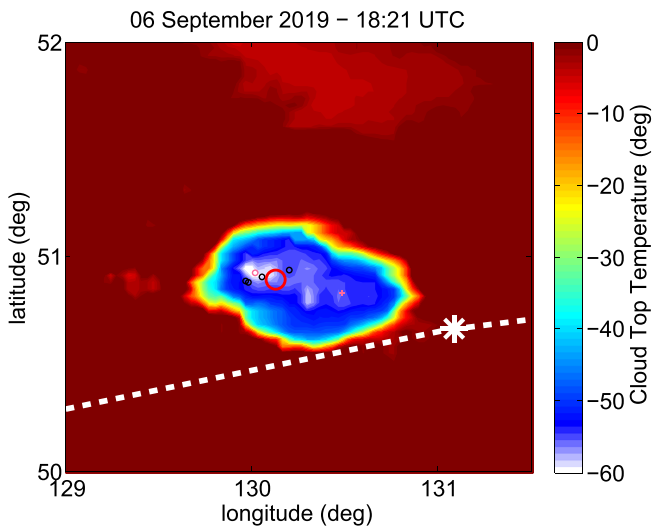


**Figure 13.** The Cloud Top Temperature infrared map, from the Himawari satellite. The circles and the pluses are the -CG and +CG strokes, respectively, detected within 5 min of the Terrestrial Gamma-ray Flashes. The red circle is the associated stroke. The dashed line shows the International Space Station trajectory and the white star marks its position at the time of the detection.

### 4.3. Event No. 9: September 6th, 2019

The event happened at 18:15:00 UTC and with a latitude of  $50.9^\circ$  it is the highest latitude event ever detected. Being at daytime, MMIA and LED data are not available. BGO lightcurve and the waveform of the associated lightning sferic are shown in Figure 12. The storm (Figure 13) is fairly compact and isolated, with a relatively low flash activity. The candidate stroke seems to come from the edge of the overshooting top. The coldest CTT is of  $-60^\circ C$ , reached a few minutes after the TGF. ENTLN, WWLLN and GLD360 report four strokes within one millisecond, all coming from the same location (see Table 2). We regard them as multiple detections of the same sferics, shown in the bottom panel of Figure 12. The associated stroke was an IC with a peak current of  $129 \pm 53$  kA, the highest in our sample according to the estimation derived from ENTLN waveform data. Given the isolated character of the storm and the clustering of the lightning activity, we identify this cluster of sferics as the stroke most probably associated to the TGF, although the ASIM absolute timing accuracy does not allow a firm association, as in the case of event no. 5.

## 5. Discussion

### 5.1. Meteorological Analysis

The 14 events we are presenting are likely following local meteorological patterns, but it is worth noticing that they all happened during the local summer or autumn. None of them happened during the local

**Table 3**  
Cloud Top Temperature (CTT, Degrees Celsius) in the Parent Storms  
Compared to the Local, Monthly Average Temperature at the Tropopause  
(TPT)

Event	$CTT_{TGF}$	CTT min	TPT avg <sup>a</sup>	CTT min-TPT avg	TPT l-t avg <sup>b</sup>	SD <sup>c</sup>
1	-60°	-70°	-64°	-6°	-62.5°	1.575°
2	-58°	-69°	-62.5°	-6.5°	-60.5°	1.425°
3	-57°	-64°	-59.5°	-4.5°	-62°	1.5°
4	-53°	-67°	-61.5°	-5.5°	-60.75°	2.3°
5	-57°	-62.5°	-56.5°	-6°	-57.5°	1.65°
6 <sup>d</sup>	-	-52°	-54.5°	2.5°	-55.5°	1.725°
7	-58°	-60°	-62°	2°	-63°	1.975°
8	-60°	-72°	-61.75°	-10.25°	-61°	1.75°
9	-56°	-60°	-54.75°	-5.25°	-54.4°	1.305°
10	-55°	-70°	-60°	-10°	-57.5°	1.85°
11	-66°	-71°	-62.25°	-8.75°	-59.65°	1.71°
12	-58°	-70°	-63°	-7°	-62.25°	1.77°
13	-62°	-70°	-65°	-5°	-62.25°	1.77°
14	-70°	-72°	-63.75°	-8.25°	-62.5°	1.7°

Note. All temperatures except the minimum CTT within the cloud system (CTT min) are calculated at the position of the parent stroke, if available. The values for the tropopause are obtained from the NCEP/NCAR reanalysis.

<sup>a</sup>Monthly average temperature for the month of the observation. <sup>b</sup>Monthly long-term average temperature, calculated over the period 1981–2010.

<sup>c</sup>Monthly interannual standard deviation of temperatures. <sup>d</sup>In the absence of an associated stroke, the position of a lightning core active in the same second was used.

winter, which may be linked to a lower frequency of convective activity in the study area, as winter convection tends to be lower above sea level, thus making it even more difficult for a hypothetical TGF to escape the atmosphere.

We analyzed the evolution of each parent storm, reconstructed using cloud top temperature data from geostationary satellites. All events except two were produced within isolated and relatively small thunderstorms. The only exceptions are event no. 1, produced in the rainband of hurricane Chris, and event no. 4, associated to extensive multicell systems. Nonetheless, all storms are convective and all except numbers 6 and 7 present an overshooting top with a CTT that is on average 5.6° colder than the monthly average temperature of the tropopause. This large difference of temperature may be due to the overshooting itself that rises above the tropopause level, but also to cold temperatures in the upper troposphere which makes favorable conditions for thunderstorm development. As shown in Table 3, the cloud top temperature in the area of the associated stroke is typically between -50°C and -60°C and, notably, it is significantly warmer than the minimum temperature, which is around -70°C in most cases. In many of the cases presented in the Supporting Information S1, the TGF is produced outside the updraft, close to the periphery of the convective region. A further hint that TGF production is not directly related to updraft activity is that some storms produce the TGF during the decaying phase, but others do it during a growing phase after a cycle of previous growth and decay. A relationship between TGF occurrence and flash rate has been previously reported, showing that the interflash rate before TGFs is longer than the average for the storm, pointing toward longer charging times (Larkey et al., 2019). These storms show varying characteristics between each other but, considering the geographic area in which they occur, none of them is particularly severe or unusual in terms of total duration, size of the convective core and total extension of the system. Some of them, like cases 6, 7 and 9, are actually weak storms. Gjesteland et al. (2015) also reports that one of the TGFs of the sample was produced by a storm with unusually weak convection. Soula et al. (2017)

reports the analysis of a very active, sprite-producing storm over the Mediterranean Sea, which we can compare to our events occurring in the same area and season (events nos. 2, 3 and 11, found in the Supporting Information S1). The reference storm had a minimum CTT of -73°C and very cold CTT in a large area and during a long period of the storm lifetime, which the authors interpret as a sign of deep convection. The minimum CTT in our cases is warmer and covers a smaller area, implying a weaker (but not weak) convection. It is also notable that convection is generally weaker over sea than it is over mainland. Exceptions to this trend are the Mediterranean Sea in autumn and the North-West Atlantic Ocean in summer and autumn, in both cases because of the warm water. Cases 6, 7 and 9 show the warmest minimum CTT among the sample, pointing toward conditions of weak convection, with case 7 not even reaching the average tropopause temperature. With the caveat that we only have 14 cases, this suggests that TGF do not seem to require unusual meteorological conditions: as long as the storm can achieve an electric field that is locally and temporarily strong enough to generate a TGF, it needs not be an extreme weather event. This result is consistent with the conclusions of Splitt et al. (2010), Chronis et al. (2016) and Ursi et al. (2019), for the first time extended to the mid latitudes. In other words, the fact that TGFs require convection, but not extreme meteorological conditions holds true at mid latitudes too. We refer to Section 5.3 for a statistical analysis of TGF occurrence.

## 5.2. Characteristics of Correlating Lightning Strokes

The peak current of the parent strokes, reported in Table 2, is between 10 and 30 kA for all events except the four ones reported below. Peak current estimation for IC lightning is difficult and imprecise for a variety of reasons (Cummins & Murphy, 2009), so global or even long-term datasets of IC characteristics are not

**Table 4**  
*Statistics of the Equatorial Regions of Interest (ROIs)*

ROI	Lon <sup>a</sup>	Lat <sup>a</sup>	flashes <sup>b</sup>	TGFs <sup>c</sup>	Avg TLR	Peak TLR	$\alpha$
C. Africa	10/30	−10/10	421,679	62	$1.47 \times 10^{-4}$	$5.17 \times 10^{-4}$	0.082
C. America	−110/−50	−5/20	341,006	144	$4.22 \times 10^{-4}$	$2.12 \times 10^{-3}$	0.080
S-E Asia	90/150	−10/20	337,452	171	$5.07 \times 10^{-4}$	$1.97 \times 10^{-3}$	0.080

<sup>a</sup>Min/max. <sup>b</sup>Number of flashes in the ROI from LIS/OTD maps multiplied by ASIM exposure time. <sup>c</sup>Number of TGFs detected by ASIM in the ROI. <sup>d</sup>Average atmospheric transmission factor.

available. Cummins and Murphy (2009) and Rakov and Uman (2007) report peak currents of around 1 kA for the K-change phase and even smaller currents for the stepping phase. From the analysis of a sample of positive polarity sferics detected by GLD360 in a  $\pm 15$  minutes interval around the trigger times of our sample and  $10^\circ$  radius around ASIM's location we find a median peak current of +6 kA. The peak current of the strokes associated to our sample are significantly higher than that, but, on the other hand, most of them cannot be classified as Energetic In-cloud Pulses (EIP) or Compact Intra-cloud Discharges (CID) either. Nag and Rakov (2010) describes a sample of CIDs with peak currents between 87 and 259 kA, with an arithmetic mean of 150 kA. Lyu et al. (2015) reports currents of 200–304 kA for CIDs and 200–584 kA for EIPs, however, we note that the 200 kA lower limit was set by the selection criteria and is not given by the physical nature of the event. Events 4, 9, 12 and 14 exhibit sferics with large peak currents possibly associated to CIDs, according to the range provided by Nag and Rakov (2010). Lu et al. (2011) report the peak current of strokes associated to a sample of RHESSI TGFs and find them to vary in the range between less than 10 and 270 kA, with a mean value of 58 kA. They do not compare these strokes to a general sample, but peak current values of a few tens of kA are consistent with our findings. They also note that all TGFs with latitude greater than  $23^\circ$  have currents smaller than 60 kA, while we instead have four events above 100 kA. They did remove NBE candidates from their sample, and they also do not provide the exact coordinates of their non-tropical events, however the possibility of a difference in average peak current between different latitudes (or geographic regions) may be worthy of further investigation. We must also remember that about 70% of TGFs are not directly associated to sferics detectable by WWLLN (Connaughton et al., 2013), therefore it is not correct to state that TGFs are in general associated to large peak currents. Our mid latitude TGFs must be intrinsically very bright to be detected despite the larger atmospheric absorption. Under the assumption that a significant fraction of the measured current is due to the TGF itself (Dwyer & Cummer, 2013), the large intrinsic brightness and short duration can explain the large peak currents observed.

All events except one have a positive sign of the peak current, which indicates negative charge moving upwards; this is consistent with previous results (Cummer, 2005). However, we remark here that the ASIM absolute timing accuracy does not allow a precise one-to-one association to a specific lightning sferic, except for cases nos. 2 and 4. Regardless of this issue, it is worth noticing that all the sferics possibly associated to the TGFs exhibit higher than average peak currents which, in one third of the cases, reach levels compatible with those reported for CIDs and, possibly, EIPs. We relied on manual examination of the waveform, particularly of the first peak, to determine the stroke type and polarity, as the automatic classification by the detection networks is not always reliable. We determined this way that all but one strokes that were reported as -IC (had a reported negative peak current) were in fact + IC. Event no. 1 was confirmed being associated to a stroke with negative current, meaning it is a -IC. This classification is shared by all ENTLN detectors that recorded the pulse and by GLD360 processed data. The TGF itself does not present any features that set it apart from the rest of the sample. It might well be that the TGF is associated to a leader step not bright enough to be detected by the lightning location networks. Given the ASIM absolute timing accuracy, we regard this event as ambiguous and we cannot further elaborate on that. Finally, we remark that, being the TGF sample selected on the basis of latitude and not on the presence of an associated stroke, it is not biased toward stronger lightning flashes or storms with more intense lightning activity.

**Table 5**  
*Statistics of the Mid Latitude Regions of Interest (ROIs)*

ROI	Lon <sup>a</sup>	Lat <sup>a</sup>	Flashes <sup>b</sup>	TGF <sup>c</sup>	w. X <sup>d</sup>	TLR 68% <sup>e</sup>	TLR 95% <sup>f</sup>
C. Europe	−10/40	35/52	226,498	3	0.37	$(1.6 / 7.1) \times 10^{-5}$	$7.4 \times 10^{-6} / 1.1 \times 10^{-4}$
N-E America	−95/−44	35/52	210,868	7	0.60	$(3.5 / 8.6) \times 10^{-5}$	$2.3 \times 10^{-5} / 1.2 \times 10^{-4}$
N-E Asia	115/144	35/52	110,270	2	0.40	$1.6 \times 10^{-5} / 1.1 \times 10^{-4}$	$5.6 \times 10^{-6} / 1.7 \times 10^{-4}$
S-E Africa	25/44	−52/−34	21,759	2	0.39	$8.5 \times 10^{-5} / 5.6 \times 10^{-4}$	$2.9 \times 10^{-5} / 8.7 \times 10^{-4}$

<sup>a</sup>Min/max. <sup>b</sup>Number of flashes in the ROI from LIS/OTD maps multiplied by ASIM exposure time. <sup>c</sup>Number of TGFs detected by ASIM in the ROI. <sup>d</sup>Weighted X: the effective lightning number divided by the total number of lightning flashes in the ROI. <sup>e</sup>TGF-to-lightning ratio at 68% confidence interval. <sup>f</sup>TGF-to-lightning ratio at 95% confidence interval.

### 5.3. Frequency of High Latitude TGFs

Table 4 shows the average and peak TLR for the equatorial regions, while Table 5 shows the observed number of TGFs and the estimated TLR for the high latitude regions. All estimates are based on calculations performed according to the procedure detailed in Section 3.3. For the three equatorial regions we obtain TLR ratios similar to the ones reported by other missions (Briggs et al., 2013; Smith et al., 2010). In particular, Briggs et al. (2013) reports the following TLR values:  $(4.9 \pm 0.3) \times 10^{-4}$  for Central America,  $(2.3 \pm 0.2) \times 10^{-4}$  for Central Africa and  $(2.7 \pm 0.4) \times 10^{-4}$  for South-East Asia, compatible with our results although the calculation procedure is slightly different. Fuschino et al. (2011) reports much lower values for the TLR over equatorial regions for AGILE, but those results were obtained before the configuration change (Marisaldi et al., 2015) which resulted in about one order of magnitude improvement in detection efficiency. The difference in the TLR, now confirmed by ASIM's data too, is well known for the three standard regions (Central America, Central Africa and South-East Asia) and discussed in depth in Fabr3 et al. (2019). For the high latitude ROIs, the 95% upper limits of the confidence levels are marginally compatible with the low-latitude values, that is, not within the two-standard deviations limit but very close to it. The case of South Africa is remarkable, as for both intervals it is more than twice the value in the other high latitude regions, and it is compatible with the value for Central Africa. This suggests that the South African ROI may be an extension of the Central African hotspot, which is in fact also inferred from the lightning maps. All other mid latitude regions have a TLR confidence level lower than the corresponding, low-latitude regions, though still marginally compatible. It seems then that for these regions a higher absorption rate may not be the only factor at play. Smith et al. (2010) also found differences in the TGF distribution at mid latitudes and the LIS/OTD maps, even after compensating for higher absorption rates. We have now confirmed this discrepancy for the regions where our samples overlap (North-West Atlantic and Mediterranean Sea) and found that it extends to the other observed ROI too. With the data that we have available, we can only point to the IC-CG ratio as a likely candidate for this discrepancy, as it is known to exhibit strong geographical variations and has been shown to be dependent on local orography (de Souza et al., 2009) and atmospheric aerosol content (Liu et al., 2020). However, de Souza et al. (2009) found no correlation with latitude, so subsequent studies will have to focus on the specific characteristics of each ROI. We point out that the transmission factor was calculated from the pressure value at tropopause altitude, even though TGFs are produced a few km below (Cummer et al., 2015). This is the explanation that Smith et al. (2010) propose for the discrepancy they report. However, the actual value for the production altitude is not known and it may well be different at low and at mid latitudes, due to the different structure that thunderstorms have in different regions. An estimate of the transmission factor for an altitude of production 3 km below the tropopause was nonetheless carried out (not shown), and it still supports the conclusions presented.

## 6. Conclusions

We presented a sample of 14 TGFs detected by ASIM above  $\pm 35^\circ$  latitude in the period from June 2018 to August 2020, including the first ever reported detections above  $\pm 38^\circ$ . The events cluster in four distinct regions: the Mediterranean Sea, the northwestern Atlantic Ocean, the coast of South Africa and north-eastern

China. A Kolmogorov-Smirnov test performed on the number of counts and the duration ( $T_{90}$ ) distributions shows significant differences in the duration with respect to the general sample (indicating that TGFs at mid latitude are typically shorter), but not in the number of counts.

The analysis of the meteorological environment point toward convective storms with overshooting cloud tops. However, these systems do not show extreme characteristics for the location: on the contrary, we mostly see compact, isolated and moderately active systems, with the TGF often produced outside of the main updraft. Although the ASIM absolute timing accuracy does not allow a one-to-one association to lightning sferics except in one case, the candidate associations are positive IC, with a current significantly higher than previously reported typical value; in four cases it may be an EIP or a CID. In one case we report only sferics of negative polarity during a time interval associated to the TGF.

The analysis of atmospheric transmission supports the idea that the rarity of TGFs at mid latitude is mostly explained by a higher absorption due to a lower tropopause height. Nonetheless, local meteorological patterns may also be at play as, for example, different IC to CG ratios. The TLR obtained at low latitudes is compatible with the one previously reported by RHESSI and Fermi, and the one estimated at high latitude is typically lower but marginally compatible with the one of the closest tropical chimney.

The ASIM data for each event are available at the following link: <https://zenodo.org/record/4727069#.YIp6VxKxVH4>

## Data Availability Statement

The NCEP/NCAR Reanalysis Derived data were provided by the NOAA/OAR/ESRL PSL, Boulder, Colorado, USA, from their Web site at <https://psl.noaa.gov/>.

## Acknowledgments

This project has received funding from the European Union's Horizon 2020 research and innovation programme under the Marie Skłodowska-Curie grant agreement 722337. The authors wish to thank Earth Networks (<https://www.earthnetworks.com/>), WWLLN (<http://wwlln.net>) and Vaisala (<https://www.vaisala.com/en>) for providing lightning data. This study was supported by the Research Council of Norway under contracts 208028/F50 and 223252/F50 (CoE). The authors thank the French AERIS/ICARE Data and Services Center which provided MSG/SEVIRI data for cloud top temperature.

## References

- Albrecht, R., Goodman, S., Buechler, D., Blakeslee, R., & Christian, H. (2016). *Lis 0.1 degree very high resolution gridded lightning climatology data collection*.
- Blakeslee, R. J., Lang, T. J., Koshak, W. J., Buechler, D., Gatlin, P., Mach, D. M., et al. (2020). Three years of the lightning imaging sensor onboard the international space station: Expanded global coverage and enhanced applications. *Journal of Geophysical Research: Atmosphere*, 125(16), e2020JD032918. <https://doi.org/10.1029/2020jd032918>
- Briggs, M. S., Xiong, S., Connaughton, V., Tierney, D., Fitzpatrick, G., Foley, S., et al. (2013). Terrestrial gamma-ray flashes in the fermi era: Improved observations and analysis methods. *Journal of Geophysical Research: Space Physics*, 118(6), 3805–3830. <https://doi.org/10.1002/jgra.50205>
- Chanrion, O., Neubert, T., Lundgaard Rasmussen, I., Stoltze, C., Tcherniak, D., Jessen, N. C., et al. (2019). The modular multispectral imaging array (mmia) of the asim payload on the international space station. *Space Science Reviews*, 215(4), 28. <https://doi.org/10.1007/s11214-019-0593-y>
- Chronis, T., Briggs, M. S., Pfriftis, G., Connaughton, V., Brundell, J., Holzworth, R., et al. (2016). Characteristics of thunderstorms that produce terrestrial gamma ray flashes. *Bulletin of the American Meteorological Society*, 97(4), 639–653. <https://doi.org/10.1175/BAMS-D-14-00239.1>
- Connaughton, V., Briggs, M. S., Xiong, S., Dwyer, J. R., Hutchins, M. L., Grove, J. E., et al. (2013). Radio signals from electron beams in terrestrial gamma ray flashes. *Journal of Geophysical Research: Space Physics*, 118(5), 2313–2320. <https://doi.org/10.1029/2012ja018288>
- Cummer, S. A. (2005). Measurements and implications of the relationship between lightning and terrestrial gamma ray flashes. *Geophysical Research Letters*, 32(8), L08811. <https://doi.org/10.1029/2005gl022778>
- Cummer, S. A., Lyu, F., Briggs, M. S., Fitzpatrick, G., Roberts, O. J., & Dwyer, J. R. (2015). Lightning leader altitude progression in terrestrial gamma-ray flashes. *Geophysical Research Letters*, 42(18), 7792–7798. <https://doi.org/10.1002/2015gl065228>
- Cummins, K. L., & Murphy, M. J. (2009). An overview of lightning locating systems: History, techniques, and data uses, with an in-depth look at the u.s. nldn. *IEEE Transactions on Electromagnetic Compatibility*, 51(3), 499–518. <https://doi.org/10.1109/TEMC.2009.2023450>
- de Souza, P., Pinto, O., Pinto, I., Ferreira, N., & dos Santos, A. (2009). The intracloud/cloud-to-ground lightning ratio in southeastern brazil. *Atmospheric Research*, 91(2), 491–499. (13th International Conference on Atmospheric Electricity) <https://doi.org/10.1016/j.atmosres.2008.06.011>
- Dwyer, J. R., & Cummer, S. A. (2013). Radio emissions from terrestrial gamma-ray flashes. *Journal of Geophysical Research: Space Physics*, 118(6), 3769–3790. <https://doi.org/10.1002/jgra.50188>
- Fabró, F., Montanyà, J., van der Velde, O. A., Pineda, N., & Williams, E. R. (2019). On the tgf/lightning ratio asymmetry. *Journal of Geophysical Research: Atmosphere*, 124(12), 6518–6531. <https://doi.org/10.1029/2018jd030075>
- Fishman, G. J., Bhat, P. N., Mallozzi, R., Horack, J. M., Koshut, T., Kouveliotou, C., et al. (1994). Discovery of intense gamma-ray flashes of atmospheric origin. *Science*, 264(5163), 1313–1316. <https://doi.org/10.1126/science.264.5163.1313>
- Füllekrug, M. (2009). Wideband digital low-frequency radio receiver. *Measurement Science and Technology*, 21(1), 015901. <https://doi.org/10.1088/0957-0233/21/1/015901>

- Fuschino, F., Marisaldi, M., Labanti, C., Barbiellini, G., Del Monte, E., Bulgarelli, A., et al. (2011). High spatial resolution correlation of agile tgfs and global lightning activity above the equatorial belt. *Geophysical Research Letters*, 38(14), L14806. <https://doi.org/10.1029/2011GL047817>
- Gjesteland, T., Østgaard, N., Laviola, S., Miglietta, M. M., Arnone, E., Marisaldi, M., et al. (2015). Observation of intrinsically bright terrestrial gamma ray flashes from the mediterranean basin. *Journal of Geophysical Research: Atmosphere*, 120(23), 12143–12156. <https://doi.org/10.1002/2015jd023704>
- Humphreys, W. (1964). *Physics of the air*. Dover Publications, Inc.
- Heumesser, M., Chanrion, O., Neubert, T., Christian, H. J., Dimitriadou, K., Gordillo-Vazquez, F. J., et al. (2021). Spectral observations of optical emissions associated with Terrestrial Gamma-Ray Flashes. *Geophysical Research Letters*, 48, e2020GL090700. <https://doi.org/10.1029/2020GL090700>
- Johnson, N. L., Kemp, A. W., & Kotz, S. (2005). Poisson Distribution. In *Univariate discrete distributions* (p. 156–207). John Wiley & Sons, Ltd. <https://doi.org/10.1002/0471715816.ch4>
- Kalnay, E., Kanamitsu, M., Kistler, R., Collins, W., Deaven, D., Gandin, L., et al. (1996). The NCEP/NCAR 40-Year Reanalysis Project. *Bulletin of the American Meteorological Society*, 77(3), 437–471. [https://doi.org/10.1175/1520-0477\(1996\)077<0437:tnyrp>2.0.co;2](https://doi.org/10.1175/1520-0477(1996)077<0437:tnyrp>2.0.co;2)
- Larkey, R. K., Sample, J. G., Smith, D. M., Briggs, M. S., Lapierre, J. L., & Holzworth, R. H. (2019). Evidence for extended charging periods prior to terrestrial gamma ray flashes. *Geophysical Research Letters*, 46(17–18), 10619–10626. <https://doi.org/10.1029/2019gl083827>
- Lindanger, A., Marisaldi, M., Maiorana, C., Sarria, D., Albrechtsen, K., Østgaard, N., et al. (2020). The 3rd agile terrestrial gamma ray flash catalog. Part i: Association to lightning sferics. *Journal of Geophysical Research: Atmosphere*, 125(11), e2019JD031985. <https://doi.org/10.1029/2019jd031985>
- Liu, Y., Guha, A., Said, R., Williams, E., Lapierre, J., Stock, M., & Heckman, S. (2020). Aerosol effects on lightning characteristics: A comparison of polluted and clean regimes. *Geophysical Research Letters*, 47(9), e2019GL086825. <https://doi.org/10.1029/2019gl086825>
- Lu, G., Cummer, S. A., Li, J., Han, F., Smith, D. M., & Grefenstette, B. W. (2011). Characteristics of broadband lightning emissions associated with terrestrial gamma ray flashes. *Journal of Geophysical Research*, 116(A3), A03316. <https://doi.org/10.1029/2010ja016141>
- Lyu, F., Cummer, S. A., & McTague, L. (2015). Insights into high peak current in-cloud lightning events during thunderstorms. *Geophysical Research Letters*, 42(16), 6836–6843. <https://doi.org/10.1002/2015gl065047>
- Marisaldi, M., Argan, A., Ursi, A., Gjesteland, T., Fuschino, F., Labanti, C., et al. (2015). Enhanced detection of terrestrial gamma-ray flashes by agile. *Geophysical Research Letters*, 42(21), 9481–9487. <https://doi.org/10.1002/2015gl066100>
- Marisaldi, M., Fuschino, F., Labanti, C., Galli, M., Longo, F., Del Monte, E., et al. (2010). Detection of terrestrial gamma ray flashes up to 40 mev by the agile satellite. *Journal of Geophysical Research*, 115(A3), A00E13. <https://doi.org/10.1029/2009JA014502>
- Nag, A., & Rakov, V. A. (2010). Compact intracloud lightning discharges: 2. Estimation of electrical parameters. *Journal of Geophysical Research*, 115(D20), D20103. <https://doi.org/10.1029/2010jd014237>
- Neubert, T., Østgaard, N., Reglero, V., Blanc, E., Chanrion, O., Oxborrow, C. A., et al. (2019). The asim mission on the international space station. *Space Science Reviews*, 215(2), 26. <https://doi.org/10.1007/s11214-019-0592-z>
- Østgaard, N., Balling, J. E., Bjørnson, T., Brauer, P., Budtz-Jørgensen, C., Bujwan, W., et al. (2019). The modular x- and gamma-ray sensor (mxgs) of the asim payload on the international space station. *Space Science Reviews*, 215(2), 23. <https://doi.org/10.1007/s11214-018-0573-7>
- Østgaard, N., Neubert, T., Reglero, V., Ullaland, K., Yang, S., Genov, G., et al. (2019). First 10 months of tgf observations by asim. *Journal of Geophysical Research: Atmosphere*, 124(24), 14024–14036. <https://doi.org/10.1029/2019jd031214>
- Rakov, V., & Uman, M. (2007). *Lightning: Physics and effects*. Cambridge University Press.
- Rodger, C. J., Brundell, J. B., & Holzworth, R. H. (2009). *Improvements in the wwlln network. bigger detection efficiencies through more stations and smarter algorithms*.
- Said, R. K., Inan, U. S., & Cummins, K. L. (2010). Long-range lightning geolocation using a vlf radio atmospheric waveform bank. *Journal of Geophysical Research*, 115(D23), D23108. <https://doi.org/10.1029/2010jd013863>
- Smith, D. M., Buzbee, P., Kelley, N. A., Infanger, A., Holzworth, R. H., & Dwyer, J. R. (2016). The rarity of terrestrial gamma-ray flashes: 2. Rhessi stacking analysis. *Journal of Geophysical Research: Atmosphere*, 121(19), 11382–11404. <https://doi.org/10.1002/2016jd025395>
- Smith, D. M., Hazelton, B. J., Grefenstette, B. W., Dwyer, J. R., Holzworth, R. H., & Lay, E. H. (2010). Terrestrial gamma ray flashes correlated to storm phase and tropopause height. *Journal of Geophysical Research*, 115(A8), A00E49. <https://doi.org/10.1029/2009ja014853>
- Smith, D. M., Lopez, L. I., Lin, R. P., & Barrington-Leigh, C. (2005). Terrestrial gamma-ray flashes observed up to 20 mev. *Science (New York, N.Y.)*, 307, 1085–1088. <https://doi.org/10.1126/science.1107466>
- Soula, S., Mlynarczyk, J., Füllekrug, M., Pineda, N., Georgis, J.-F., van der Velde, O., et al. (2017). Dancing sprites: Detailed analysis of two case studies. *Journal of Geophysical Research: Atmosphere*, 122(6), 3173–3192. <https://doi.org/10.1002/2016jd025548>
- Splitt, M. E., Lazarus, S. M., Barnes, D., Dwyer, J. R., Rassoul, H. K., Smith, D. M., et al. (2010). Thunderstorm characteristics associated with rhessi identified terrestrial gamma ray flashes. *Journal of Geophysical Research*, 115(A6), A00E38. <https://doi.org/10.1029/2009ja014622>
- Ursi, A., Marisaldi, M., Dietrich, S., Tavani, M., Tiberia, A., & Porcu, F. (2019). Analysis of thunderstorms producing terrestrial gamma ray flashes with the meteosat second generation. *Journal of Geophysical Research: Atmosphere*, 124(23), 12667–12682. <https://doi.org/10.1029/2018jd030149>
- Williams, E., Boldi, R., Bór, J., Sántori, G., Price, C., Greenberg, E., et al. (2006). Lightning flashes conducive to the production and escape of gamma radiation to space. *Journal of Geophysical Research*, 111(D16), D16209. <https://doi.org/10.1029/2005jd006447>